Inherited Crustal Features and Southern Alaska Tectonic History Constrained by Sp Receiver Functions

Michael Everett Mann[1], Karen M. Fischer[1], Jeff Apple Benowitz[2]

[1] Department of Earth, Environmental and Planetary Sciences, Brown University, Providence, RI, USA
[2] GeoSep Services, 1521 Pine Cone Road, Moscow, ID, USA
Corresponding author: Michael Everett Mann (michael_mann@brown.edu)

Abstract

Southern Alaska is a collage of fault-bounded accreted terranes. The deformation history of these crustal blocks and geometric history of the bounding faults reflect both inherited features and subsequent convergent margin events. Multiple dense (<20-km spacing) arrays of broadband seismometers across southern Alaska has previously allowed for imaging of crustal structure across the region using various seismic imaging methods. Here, we employ S-to-P receiver functions to investigate the crustal structure of southern Alaska for signals of dynamic tectonic activity. The subduction zone plate interface and subducting slab Moho are imaged dipping at shallow (<60-km) depths across the southernmost part of the subduction zone. Along two different transects, an inboard-dipping (~15°) boundary is imaged intersecting the trace of the Border Ranges Fault at the surface that we infer represents an unrotated inboard-dipping paleo-subduction (Mesozoic) interface. This observation is combined with previous seismic imaging along both the Border Ranges Fault and the next seaward terrane-bounding fault—the Contact Fault—to buttress a known history of convergent tectonics that varies along the margin. Along with large (>10-km) crustal thickness offsets imaged across both the Denali Fault system and the

Eureka Creek Fault, this feature supports a Mesozoic-to-Present inboard-dipping (east and northward) subduction polarity in the region. Additionally, the Sp CCP volume reveals a 100-km x 50-km sized positive velocity gradient with depth (PVG) at ~25-km depth beneath the Copper River Basin, which we interpret as the top of a region of active underplating and/or intrusion of basaltic magmatism into the lower crust. This feature may be related to the generation of a new Wrangell Volcanic Field volcano, resulting from the underlying tear in the subducting slab.

1. Introduction

Continental crust is a palimpsest of tectonic activity, where ancient terrane boundaries and convergent margin structures can persist for 10's of millions of years (e.g., Korja & Heikkinen, 2008; Hopper et al., 2017; Long et al., 2019; Li et al., 2020). Thus, imaging crustal architecture can help piece together the inherited and deformation history of a region (e.g., Fuis et al., 2008; Korja & Heikkinen, 2008). Southern Alaska has been a convergent margin since at least the Jurassic, leading to a tectonic quilt of Mezo-Cenozoic tectonostratigraphic accreted terranes (e.g., Nokleberg et al., 1985; Plafker & Berg, 1994). Furthermore, because of successive periods of crustal-scale strike-slip faulting parallel to the western North America margin and dissecting southern Alaska, these accreted terranes have been transported large distances (>1000 km) along the margin of western North America through time (e.g., Tikoff et al., 2023). Hence the region is a prime location to investigate inherited versus developed tectonic features, how structural architecture can be preserved through subsequent accretion events, and how these processes are expressed in seismic velocity structure.

Teleseismic scattered-wave imaging has been used for decades to investigate the crustal structure of southern Alaska (e.g., Ferris et al., 2003; Rondenay et al., 2008; Kim et al., 2014;

Miller et al., 2018; Zhang et al., 2019; Mann et al., 2022; Gama et al., 2022a). Body waves incident on velocity gradients, such as the Moho, generate scattered waves which can be extracted from within the P-coda (for incident P waves) or preceding the S-wave arrival (for incident S waves) through deconvolution, resulting in receiver functions (RFs; e.g., Langston, 1977; Farra & Vinnik, 2000). Analysis of these S-to-P scattered phases as measured in RFs (i.e., Sp RFs) has often been aimed at subhorizontal Moho and lithospheric discontinuities (e.g., Lekić et al., 2011; Gama et al., 2022a), although Sp RFs have also been used to image dipping modern and paleo structural features, for example in subduction zones (e.g., Kawakatsu et al., 2009; Kumar & Kawakatsu, 2011).

For this study, a recently developed Sp RF common-conversion point (CCP) stacking imaging procedure (Hua et al., 2020a) was applied to teleseismic S-waves recorded on dense seismometer arrays across southern Alaska (Figure 1). This Sp CCP volume reveals inboard-dipping features extending to depth from the surface trace of the Border Ranges Fault system (BRF) that potentially are associated with the Mesozoic paleo-subduction zone when a subduction interface was located along the BRF (e.g., Trop and Ridgway, 2007). We integrate our new results with previous seismic imaging work on the BRF and Contact Fault (e.g., Stephens et al., 1990; Fuis et al., 1991; Ye et al., 1997) to investigate along-strike variations in paleo-subduction interface preservation and modification (e.g., its rotation towards vertical dip), as well as linked contractional histories. Sharp Moho offsets across terrane-bounding faults including the Denali Fault and Eureka Creek Fault are also imaged. Additionally, the Sp CCP volume reveals a 100-km x 50-km sized positive velocity gradient with depth (PVG) at ~25-km depth beneath the Copper River Basin. Combined with recent seismic analyses across the region,

this mid-crustal discontinuity coincides with a dense cluster of earthquakes and may represent active underplating and/or intrusion of basaltic magmatism into the lower crust, rising from a tear in the subducting Yakutat slab which is located directly beneath this discontinuity (Mann et al., 2022; Brueseke et al., 2023).

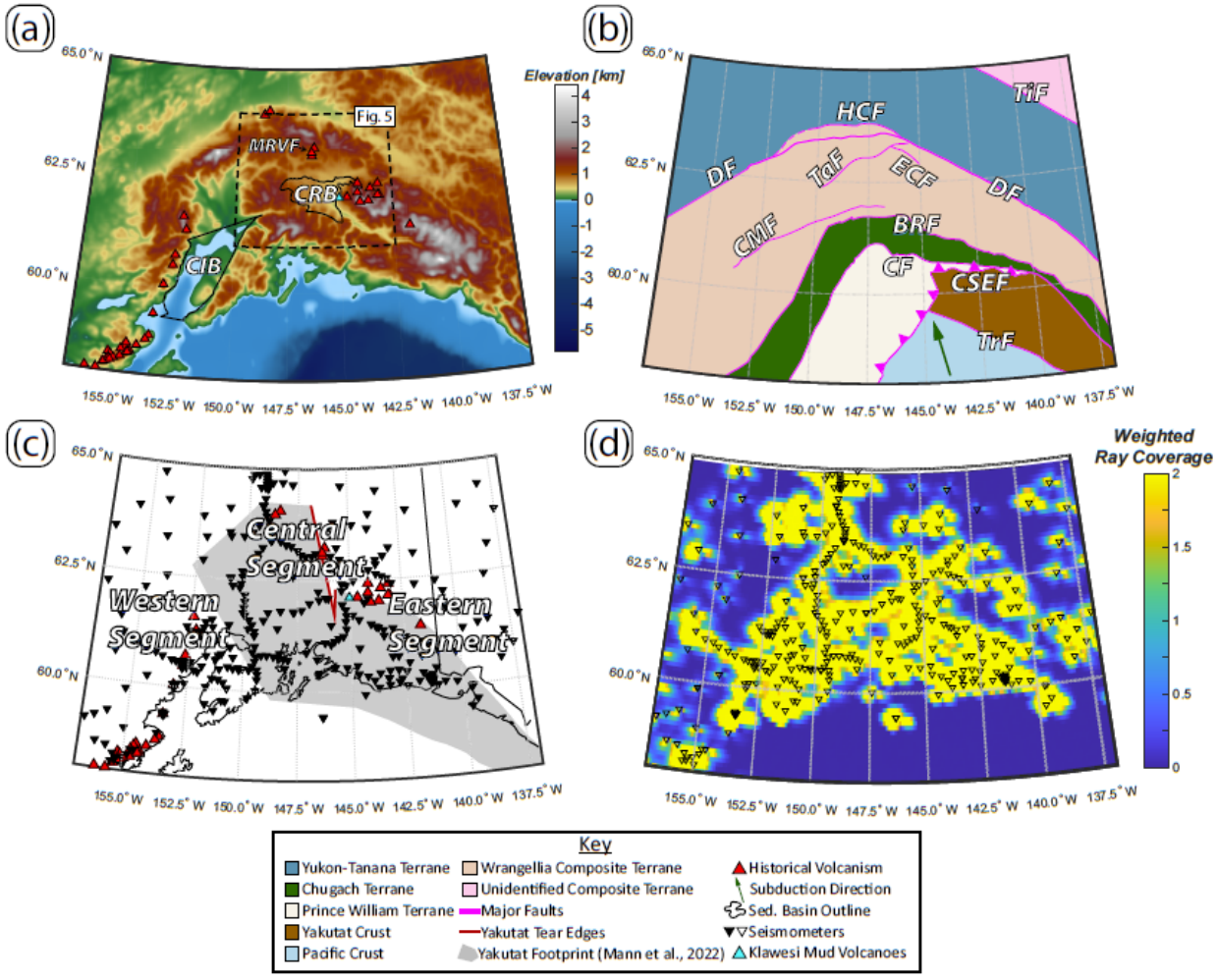

Figure 1: Overview of study area. (a) Topographic map of study region showing volcanoes and two major sedimentary basins discussed in the text. CIB–Cook Inlet Basin. CRB–Copper River Basin. MRVF–Maclaren River Volcanic Field (Brueseke et al., 2023). Outline of Figure 5 is depicted with dashed black lines. (b) Terrane map of study region showing major faults. TiF–Tintina Fault, DF–Denali Fault, HCF–Hines Creek Fault, TaF–Talkeetna Fault, CMF–Castle Mountain Fault, BRF–Border Ranges Fault, CF–Contact Fault, CSEF–Chugach-St. Elias Fault, TrF–Transition Fault, ECF–Eureka Creek Fault. (c) Location of seismic stations used in this study. Outline of Yakutat oceanic plateau shown in shaded gray, with tear highlighted in dark red. Approximate delineation of three segments (i.e., western, central, and eastern) is shown. (d) Weighted ray coverage at 50-km depth in the Sp CCP volume. We only interpret along cross sections where the weighted ray coverage is greater than 0.4.

2. Geologic Background

The accretion of the Wrangellia composite terrane (WCT) to North American affinity crust was the largest addition of crust to the continent in the last 200 million years (Trop and Ridgway, 2007). The generally accepted model is that the WCT, primarily oceanic plateau crust (Greene et al., 2010), collided along North America's western (east-dipping) subduction margin

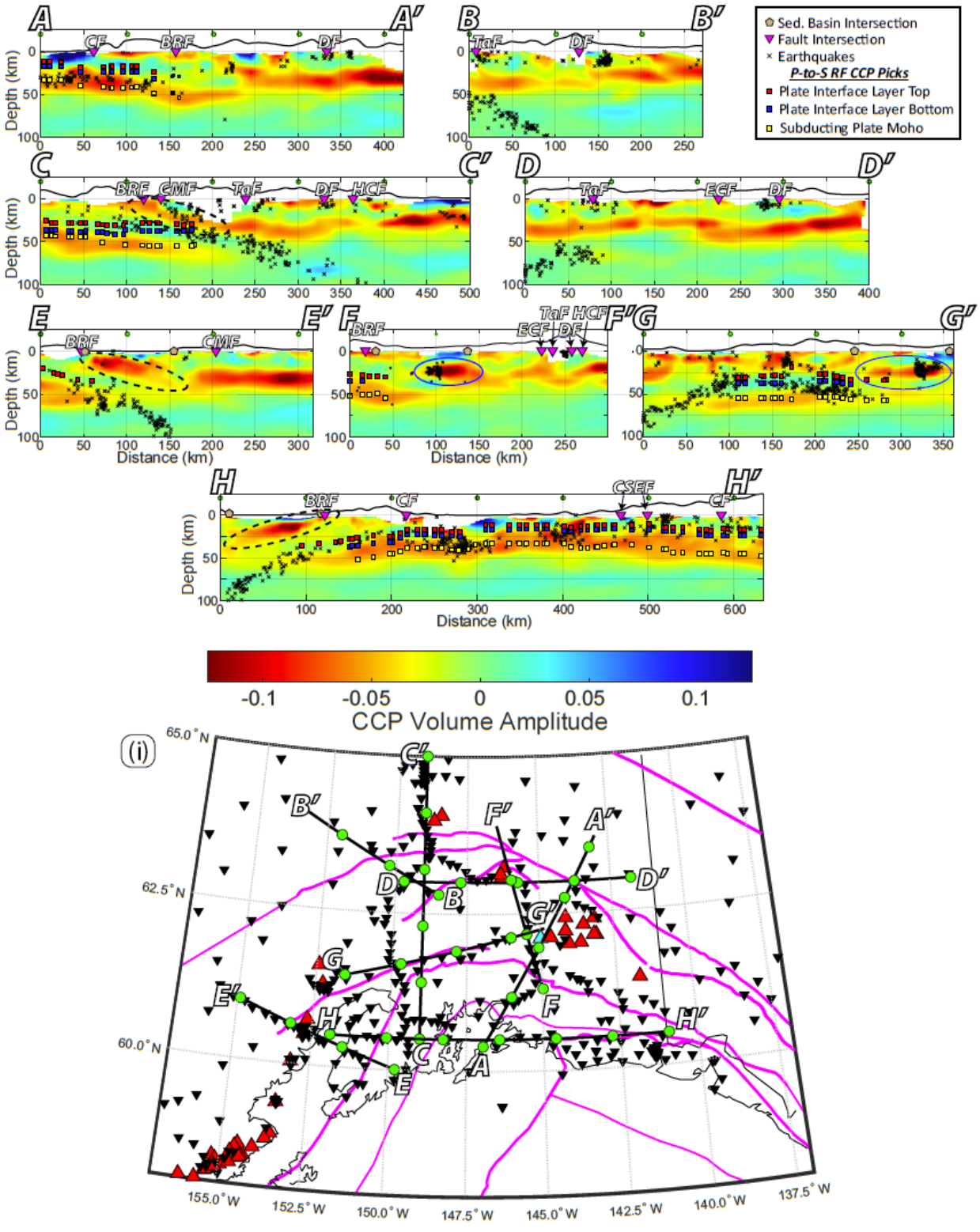
A
A′
B
B′
C
C′
D
D′
E
E′
F
F′
G
G′
H
H′
CF
BRF
DF
TaF
HCF
CMF
ECF
CSEF
Depth (km)
Distance (km)
Sed. Basin Intersection
Fault Intersection
Earthquakes
P-to-S RF CCP Picks
Plate Interface Layer Top
Plate Interface Layer Bottom
Subducting Plate Moho
-0.1
-0.05
0
0.05
0.1
CCP Volume Amplitude
(i)
65.0°N
62.5°N
60.0°N
155.0°W
152.5°W
150.0°W
147.5°W
145.0°W
142.5°W
140.0°W
137.5°W

Figure 2: Cross sections through the Sp CCP volume analyzed in this study. *Negative CCP stack amplitudes correspond to positive velocity gradients (PVG) and positive stack amplitudes correspond to negative velocity gradients (NVG). Each cross section is referenced as its own figure component, corresponding to the first letter of each line. For example, line A-A' is "Figure 2a". Small red, blue, and yellow squares plotted on each cross section are from Mann et al. (2022) Ps RF CCP imaging of the subducting Yakutat crust across the same region, using mostly the same seismometers. Small x's are earthquake hypocenters within 5 km of the cross section. Hypocenter locations are from Daly et al. (2021) to the east of 149°W (where they reported high-quality hypocenters), and from the Alaska Earthquake Center catalog to the west of 149°W. The locations where major faults (Figure 1b) cross each cross section are marked with an inverted magenta triangle and label. The locations where the lines cross the Copper River and Cook Inlet basins (Figure 1a) are in tan pentagons, plotted at z = 0 km. All fault labels (black and white lettering) are from Figure 1b. Blue ovals highlight the PVG discussed in Section 5.2.4. Black dashed ovals highlight PVG signal seen dipping inboard from the BRF. Green circles along cross sections denote locations along lines on map in part (i).*

at around ca. 100 Ma and then was translated >2000 km north along margin-parallel strike-slip fault systems (e.g., Tikoff et al., 2023). The Alaska Range suture zone (Ridgway et al., 2002; Trop et al., 2019) is the suture region between the WCT and rocks of North American affinity to the north (Figure 1). The Denali Fault System (Amand, 1957) delineates the northern boundary of the Alaska Range suture zone (Trop et al., 2019, 2020), and the Talkeetna Fault delineates the southern boundary of the Alaska Range suture zone (Brennan et al., 2011).

By ca. 50 Ma, the Chugach-Prince William Terrane had been translated north and accreted into place south of the BRF of southern Alaska (Figure 1) (Freeland & Dietz, 1973; MacKevett & Plafker, 1974; Cowan, 2003; Garver and Davidson, 2015). The Contact Fault delineates the suture between the Chugach and Prince William Terrane (Fisher & Magoon, 1978; Nilsen & Zuffa, 1982). Both the BRF and Contact Fault were likely originally subduction megathrusts which later experienced strike-slip motion (Plafker et al., 1989; Fuis et al., 1991; Bol and Roeske, 1993; Brocher et al., 1994; Bruhn et al., 2004; Trop and Ridgway, 2007). The BRF system has experienced at least ~700 km of slip between ca. 58 Ma and 50 Ma (Smart et al., 1996) playing a role in the northward translation of the Chugach-Prince William Terrane, whereas the Contact Fault experienced an undetermined amount of strike-slip motion during the Eocene and during more recent times (e.g., Bol and Roeske, 1993; Chapman et al., 2012).

The most recent accretion event affecting southern Alaska involves the Yakutat microplate which is a buoyant oceanic plateau with between 11-km (northern subducted leading edge) and 30-km thick crust (south-east outboard segment) (e.g., Eberhart-Phillips et al., 2006; Rondenay et al., 2008; Christeson et al., 2010; Worthington et al., 2012; Mann et al., 2022). Crustal thickness also varies west (~17 km) to east (~30 km) (Figure 3) (Worthington et al., 2012).

The Wrangell Arc is linked to the initiation of shallow-slab subduction of the Yakutat oceanic plateau (ca. 30 Ma; Brueseke et al., 2019). The arrival of the Yakutat slab at Alaska's southern convergent margin is also associated with deformation and mountain building across much of southern Alaska (Abers, 2008; Enkelmann et al., 2010; Arkle et al., 2013; Benowitz et al., 2019; Terhune et al., 2019).

The Neogene Yakutat "flat" slab subduction (Pavlis et al., 2004; Eberhart-Philips et al., 2006; Enkelmann et al., 2010) and true Yakutat collision (Gulick et al., 2007; Brueseke et al., 2023) has also had a profound impact on the evolving structural configuration of the St. Elias syntaxis region (eastern segment) (Figure 1c; e.g., Koons et al., 2010; Spotilia & Berger, 2010; Jadamec et al., 2013; Enkelmann et al., 2015a). During the last ~3 Ma, faults with historically primarily strike-slip kinematics experienced significant dip-slip motion (Berger et al., 2008; Pavlis et al., 2012; Schartman et al., 2019). The St. Elias region deformation front may also have shifted trenchward toward the south (Enkelmann et al., 2015a; Schartman et al., 2019).

The dynamic nature of the St. Elias syntaxis region has led to much debate on not only which faults are active and reactivated through time in this region, but also the orientation-kinematics of these structures (e.g., Bruhn et al. 2012). These concerns are compounded by some

authors referring to the far-eastern contact fault as the Contact fault (e.g., Bruhn et al., 2004), others referring to the far-eastern contact fault as the Bagley fault (Bruhn et al., 2012), and still others having the Bagley fault and Contact fault being different structures (Berger et al., 2008; Chapman et al., 2012). Though beyond the spatial resolution of our results (estimated at ~10 km laterally at Moho depths; e.g., Lekić et al., 2011) to resolve these <5-km scale mapping concerns, we feel confident assuming that the Contact fault and the BRF are not back thrusts, because this would imply these paleo-subduction interfaces have been overturned significantly.

3. Data and Methods

The southern Alaska subduction zone has seen the deployment of multiple dense (<~20-km spacing) broadband seismometer arrays that cover most of the road system (Ferris et al., 2003; Li et al., 2013; Bauer et al., 2014; Tape et al., 2017; Daly et al., 2021). These dense arrays, supplemented with other permanent stations and smaller temporary arrays, provide excellent station density across the shallow subduction zone and allow for imaging of continuous features along-strike over hundreds of kilometers (e.g., Bauer et al., 2014; Kim et al., 2014). Recent P-to-S RF (Ps RF) imaging across southern Alaska (Mann et al., 2022) has revealed the continuity and subduction of the Yakutat oceanic plateau across the region, a thin low-velocity zone along the plate interface atop the subducting Yakutat crust, and a North-South trending tear in the subducting slab below ~50-km depth (Brueseke et al., 2023). This newly imaged tear (Mann et al., 2022) has a broadly similar orientation, but a different location than the tear inferred by Fuis et al. (2008).

In this study, teleseismic S-waves recorded on seismometers across southern Alaska (Figure 1) were used to analyze the S-to-P scattered wavefield for crustal structure. Compared to

Ps RFs, there are several advantages to using Sp RFs for regional seismic imaging. First, the conversion points are farther from the stations and can provide higher-fold imaging between stations that are spaced too far apart for overlapping Ps RF Fresnel zones at upper-plate depths. Second, Sp RFs contain one scattering mode (Figure 2), whereas Ps RFs record a superposition of multiple scattering modes resulting from surface-reflected and back-scattered phases (e.g., Rondenay, 2009). Additionally, sedimentary basin multiples can obscure part of the record in Ps RFs (e.g., Sheehan et al., 1995; Cunningham & Lekić, 2019), but large basin multiples arrive after the S-wave arrival and therefore do not cause "ringing" in Sp RFs.

To generate the Sp common conversion point (CCP) volume, S-wave data were analyzed following the procedure of Hua et al. (2020a). To improve vertical resolution of the Moho and other crustal velocity gradients, waveform data were filtered with a 2 s to 30 s bandpass filter. We chose this filter to highlight crustal structure, in contrast to the Sp CCP stacking of Gama et al. (2022a), which employed a similar approach with a longer period bandpass (2 s to 100 s) in order to optimize imaging of mantle structure. Particle motion analysis of the beginning of the P- and S-waves on the P- and SV- components, respectively, was conducted to estimate "surface" velocities at each station, and was used with a free-surface transform (Kennett, 1991) to isolate the incident S wave from the converted P waves. All teleseismic S waves (Figures 1) recorded by the stations between 06/01/1999 and 04/19/2020 were analyzed, and events that had SV-components with signal-to-noise ratio > 1.5, defined as the ratio of the average within a 5 s signal window to that within a 25 s noise window, were used to generate Sp receiver functions (RFs). The resulting Sp RFs were migrated to their common conversion points using a regional 3D shear-velocity (Vs) model (Feng & Ritzwoller, 2019) and a 3D compressive-wave velocity

(Vp) model generated from that 3D Vs model with shallow (<60 km) Vp/Vs constrained by receiver function phase stacking (Mann et al., 2022). The Vp/Vs for all points below the phase stacking depth were taken at each depth from the AK135 velocity model (e.g., Kennett et al., 1995). The Sp RFs were stacked on a 3D grid of nodes (0.1° longitude x 0.1° latitude x 0.5 km in depth). At a given depth, the weighting of individual RFs at each point was determined with a horizontal Fresnel zone approximation based on 3D Sp RF isochrons plus geometrical spreading, and assuming non-zero weights only within the area where the "isochron slope angle" was less than 12° (see Hua et al., 2020a for full explanation).

Two other quality control parameters were used to cull the set of Sp RFs before stacking. First, Sp RFs that did not have a prominent negative-amplitude (associated with a positive-velocity gradient, PVG) Moho phase between 10-km and 60-km depth were excluded (following Hua et al., 2020a). In Sp RFs, the most prominent phase is associated with the Moho, and even though the upper plate Moho in subduction zones sometimes disappears or inverts in RF polarity (e.g., Bostock et al., 2002), we found that this step considerably improved the clarity of observed features in the CCP stack. Second, Sp RFs with anomalously high amplitudes in the mantle depth range were removed. Mantle velocity gradients are not expected to exceed those typically observed at the Moho (e.g., Krueger et al., 2021), so for times corresponding to the depth range of 100-450 km, Sp RFs with root mean square values greater than 0.2 were eliminated. These quality control steps resulted in 76,772 Sp RFs at the 734 stations, with an average of 105 per station. We use stations across a wider region of southern Alaska for our analysis, but we do not interpret results outside the regions of dense station spacing (Figure 1d, Figure 2). Following Hua et al. (2020a), after stacking the Sp RFs at depth, interpretation of features was limited to the

region with higher sampling, i.e., where the weighted stack value (Figure 1d; equation 27 from Hua et al., 2020a) is greater than 0.4.

Resolution for RF signals depends on frequency content and velocity along the scattered-wave ray path (e.g., Rondenay, 2009). Assuming a minimum signal period of 2 s, Sp scattered-phase wavelengths at Moho depths should be 8-9.8 km (at the crust-mantle interface depths, Vs = 4.0-4.8 km/s), and vertical resolution for imaging subhorizontal discontinuities is therefore approximately 4-4.8 km, assuming that vertical resolution from converted waves is approximately half a wavelength (Bostock, 1999).

Dip resolution for Sp CCP stacking is more difficult to quantify because it depends on a number of factors, including station spacing and distribution, the ray parameter and back-azimuthal ranges of incident S-waves, signal-to-noise, and the presence of adjacent boundaries. Overall, the shape of Sp RF sensitivity kernels yields better resolution of subhorizontal features (e.g., Hansen & Schmandt, 2017; Hua et al., 2020). However, tests with synthetic data show that shallow-dipping (<~15°) intracrustal boundaries have been imaged using Sp CCP stacking along dense lines of stations (e.g., Hopper et al., 2017). At mantle depths, dip-resolution tests using CCP stacking of synthetics indicate that dipping boundaries are resolvable up to dips of 10-15° (Lekić & Fisher, 2017; Hua et al., 2020a). Even though this maximum resolvable dip (i.e., ~15°) may be an underestimate at crustal depths, we do not interpret features with apparent dips >~15°.

4. Results

The Sp CCP volume contains clear features that represent conversions from the Moho and intracrustal interfaces. We categorize each velocity gradient interpreted here as a negative velocity gradient (NVG; velocity decreasing with depth) or positive velocity gradient (PVG;

velocity increasing with depth) instead of using RF polarity or CCP amplitude. PVGs correspond to negative Sp RF amplitudes (the convention used in the figures in this paper), although in some other studies the sign of Sp amplitudes were flipped to match the association of PVGs with positive Ps amplitudes.

The most prominent feature in the Sp CCP volume is a consistent PVG in the upper 20-65 km depth range everywhere in the CCP volume. This PVG can be divided into two regions. In the south where subduction is occurring, the PVG strikes roughly parallel to the trench and dips inboard, and likely represents the Moho of the modern subducting slab. This interpretation is supported by the continuity of the PVG with the dipping seismicity associated with the subducting slab (Figure 2a,c,e,h). Across the remaining region, the PVG is subhorizontal between 20-50 km depth with some sharp offsets in depth and corresponds with the upper-plate Moho (Figure 2). In the southern subduction region, a NVG overlies and parallels the dipping PVG at depths < 50 km nearly everywhere. This feature is likely the plate interface between subducting and overriding crust.

Other imaged features exist within the upper-plate crust across the region. At the western end, inboard-dipping PVGs extend from the surface to upper-plate Moho depths beneath the Kenai Peninsula and the region just to the north of the Kenai Peninsula (Figure 2c,e,h). These dipping PVGs intersect the surface at the trace of the BRF (Pavlis, 1982), but only exist along the western segment of the BRF system (west of ~149°W). Additionally, a strong subhorizontal PVG is imaged at ~25-km depth beneath the northern/northeastern portion of the Copper River Basin (Figure 2f,g). This PVG extends for over 100-km East-West (between 147°W and 145°W) and ~50-km North-South (between 62°N and 62.5°N). At this PVG's southeastern corner, the

feature coincides with a dense cluster of earthquakes between 15-30 km depth (Figure 2f,g; Daly et al., 2021) directly beneath the Klawasi group mud volcanoes (Figure 1) which have mantle fluid isotopic signatures, are linked to an inferred deep-seated magmatic intrusive, and are located ~20 km to the west of the main Wrangell Volcanic Arc (Figure 1; Motyka et al., 1989; Brueseke et al., 2019).

5. Discussion

5.1 The Subducting Yakutat Crust

The subducting Yakutat Moho is imaged nearly everywhere as an inboard-dipping PVG that agrees well with previous Ps RF imaging (Mann et al., 2022) (Figure 2a,c,e,f). Along line G-G', which is roughly along-strike of the subducting Yakutat slab, the top and bottom of the western half of the Yakutat crust are imaged at ~40- and ~60-km depth, respectively. This provides further evidence that the Yakutat is subducting at a very shallow angle between 150°W and 147.5°W (Figure 2g), and this result matches the Ps RF imaging across the region quite well (e.g., Mann et al., 2022).

The plate interface is imaged as a NVG nearly everywhere atop the subducting Yakutat plateau in the Sp CCP imaging and parallels the Yakutat Moho (Figure 2). This NVG is co-located with a thin LVL imaged atop the subducting Yakutat crust across the region using higher-resolution Ps RF phases (e.g., Kim et al., 2014; Mann et al., 2022). The Sp RF phases used here have slightly less volumetric resolution than the upgoing P-to-S analog conversion ("Pxs"), and significantly less resolution than surface-reflected, back-scattered RF phases. The fact that the plate interface appears as a single NVG here with lower Sp RF resolution (c.f. Mann et al., 2022) suggests that the top boundary of the LVL generates a converted wave with greater

amplitude than the bottom boundary of the LVL, and destructive interference between the two converted waves results in a single apparent NVG. The top of the LVL being a stronger velocity contrast is consistent with high resolution local earthquake scattering analysis (e.g., Kim et al., 2019). Additionally, Ps RF migration images using only Pxs show a NVG across the top of the subducting crust where the higher-resolution surface-reflected RF phases show a thin low-velocity zone (e.g., Kim et al., 2014; Mann et al., 2022).

This single NVG along the plate interface resembles structures documented in subduction zones with thinner subducting crust (<10 km; e.g., Audet et al., 2009; Abers et al., 2009) than the Yakutat slab (11-30 km; Ferris et al., 2003; Rossi et al., 2006; Rondenay et al., 2008; Worthington et al., 2012; Christeson et al., 2013; Kim et al., 2014; Mann et al., 2022), and raises a long-debated question as to what this imaged feature represents. At these depths, the velocity of the overriding crust should be lower than in the subducting basalt, so a NVG at the interface between these two features is not expected without the presence of sediment and tectonically eroded material along the interface (e.g., Abers et al., 2009; Kim et al., 2014; Mann et al., 2022) or significant porosity and pore-fluids (e.g., Peacock et al., 2011). Additionally, high-resolution seismic tomography models do not show a decrease in velocity across the interface, suggesting that the cause of the NVG is either too thin or too sparse to image completely (e.g., Calvert et al., 2020). Given the fact that Sp RFs have lower resolution than Ps RFs, and the subduction zone structure in this region has been extensively studied using Ps RFs (e.g., Kim et al., 2014; Mann et al., 2022), we only show the Ps RF CCP volume picks for the plate interface LVL and subducting Moho for comparison and to reinforce the crustal imaging results discussed below.

5.2 Upper-Plate Crustal Structure

We interpreted cross sections of the Sp CCP volume for crustal thickness and internal structure along paths that follow dense station spacing across the region. These cross sections are compared with the locations of other features, such as major faults, terrane boundaries, and earthquakes (Figure 2).

5.2.1 Border Ranges Fault

The BRF separates the inboard WCT from the seaward Chugach-Prince William Terrane (Pavlis, 1982) and is one of the most identifiable topographic surface features across Southern Alaska (Figure 3). The BRF began as a paleo-subduction zone plate interface that accommodated northward subduction beneath the Wrangellia composite terrane from Early Jurassic to Late Cretaceous time (e.g., Pavlis & Roeske, 2007; Trop & Ridgeway, 2007). Only scattered remnants of this paleo-subduction interface are still identifiable at the surface. The BRF system now consists of several branches that have juxtaposed different rock packages at different times (Plafker et al., 1989).

An inboard-dipping PVG extends from the surface trace of the BRF to >25-km depths across the northern and western sides of the Kenai Peninsula (Figure 2c,e,h). The North-South line C-C' shows this feature dipping to the north at ~15° extending from the BRF at the surface to the continental Moho (Figure 2c). Along lines E-E' and H-H', a similar feature dips to the west at ~15° beneath the Cook Inlet Basin (Figure 2e,h). We considered three geologic features that may be related to this PVG. (1) The PVG may be the top of accreted, high-velocity ultramafic-mafic rocks of the Border Range ultramafic and mafic assemblages which lie along the BRF system (e.g., Clark, 1973; Plafker et al., 1989; Kusky et al., 2007). (2) the PVG may be a sliver of Border Range ultramafic and mafic assemblages at shallow depths followed by the

top of a subhorizontal serpentinized body in the lower crust seen at ~15 km depth beneath the southeastern part of Cook Inlet Basin(Mankhemthong et al., 2013). (3) the PVG is a signal from the base of the ~5-7-km thick Cook Inlet Basin (Shellenbaum et al., 2010).

If the inboard-dipping PVG is the top of a serpentinized body, then the serpentinization could have resulted from fluid interaction within the overriding crust when the BRF was the subduction interface. However, serpentinization decreases seismic velocities (e.g., Bostock et al., 2002), so RF phases with the opposite polarity (i.e., NVG) may be expected, depending on the degree of serpentinization (Hyndman & Peacock, 2003). While the inboard-dipping PVG does not preclude serpentinization of the lowermost crust below the Kenai Peninsula and Cook Inlet Basin (e.g., Mankhemthong et al., 2013), it is unlikely that such a strong PVG could result from the top of a serpentinized body at these shallow crustal depths.

If the PVG is the base of the overlying Cook Inlet Basin, then this PVG is simply an imaging artifact. However, the geometry of the PVG is inconsistent with this interpretation. Sp RF phases are expected from the base of the overlying Cook Inlet Basin, but such arrivals would likely be subhorizontal across much of the basin (Shellenbaum et al., 2010; Kim et al., 2014; Smith & Tape, 2020). For example, the base of the ~5-7-km thick Cook Inlet Basin (Shellenbaum et al., 2010) should create a subhorizontal PVG from x = 0-120 km on line H-H'. However, the apparently subhorizontal part of the PVG only exists in the southeastern end of the basin, even though a subhorizontal PVG segment is expected throughout the basin given that there is more than sufficient station coverage (Figure 2e,h). The inboard-dipping PVG seems to continue beneath the basin to depths > 25 km. Moreover, the PVG is seen both outside the

boundary of Cook Inlet Basin (line C-C') and within the basin (lines E-E' and H-H'). Therefore, we do not think the dipping PVG is the result of artifacts from basin conversions.

We prefer the interpretation that the PVG feature is related to the inboard-dipping Mesozoic paleo-subduction interface along the BRF system between the inboard WCT and Border Range ultramafic and mafic assemblages (Clark, 1973; Kusky et al., 2007; Pavlis et al., 2019), with the Cook Inlet Basin conversions superimposed over this PVG feature in the Sp CCP volume along lines E-E' and H-H'. The next seaward terrane boundary, the Contact Fault (Figure 1b), has shallow, inboard-dipping structures beneath it as well (e.g., Fisher et al., 1983; Stephens et al., 1990; Ye et al., 1997; Eberhart-Phillips et al., 2006) although they are too shallow and/or small-scale to image with the Sp data in this study.

Both the BRF and Contact Fault were reactivated and experienced strike-slip motion during the Paleocene-Eocene (Bol & Roeseke et al., 1993; Pavlis & Roeseke, 2007; Berger et al., 2008). It has been documented that paleo-subduction interfaces can experience strike-slip motion without reorganization or rotation towards vertical of deep structure (e.g., Sato et al., 2015). However, the preservation of low-angle dip of the BRF paleo-subduction interface along the western segment (i.e., Kenai Peninsula) may in part explain why major strike-slip Eocene displacement (Garver and Davidson, 2015) was transferred onto other structures (Pavlis and Roeseke, 2007). Strike-slip along the western BRF region may have been accommodated on the nearby Eagle River Fault (Amato et al., 2013; Garver personal communication**)** and/or the Castle Mountain Fault (Pavlis & Roeseke, 2007).

There are no apparent shallow-dipping features in this CCP volume to the east of ~149°W, where the buoyant Yakutat oceanic plateau has been subducting since ca. 30 Ma (e.g.,

Brueseke et al., 2019). This could mean that the dip of the BRF has been rotated towards vertical through extensive contraction and is now dipping too steeply to image with Sp CCP stacking (e.g., Enkelmann et al., 2010; Arkle et al., 2013; Mankhemthong et al., 2013).

The BRF east of ~149°W may have been (partially?) rotated towards vertical during the oblique transport and accretion of the Chugach and Prince William Terranes. Conversely, if contraction related to buoyant Yakutat subduction is in part the reason for the absence of the imaged BRF paleo-subduction interface, the Contact Fault paleo-subduction interface managed to be preserved at least to 145.2°W with an inboard dip of ~30° under the central segment (Figure 3), as seen in active-source seismic studies (e.g., Fuis et al., 1991). The lithological similarities of the Chugach and Prince William Terranes (deep-water turbidites both sides of the Contact Fault) may in part explain why west of 145.2°W the Contact Fault was not rotated compared to the BRF (deep-water turbidites to the south, oceanic plateau-island arc to the north), which has a greater across-strike change in crustal properties (Trop and Ridgway, 2007; Mankhemthong et al., 2013).

To further investigate the relationships between upper-plate deformation and the inferred along-strike variation in dips of the BRF and Contact Faults, we measured along-strike variations in topography by averaging values within 5 km of each terrane-bounding fault near the subduction zone (i.e., BRF, Contact Fault, and Chugach-St. Elias Fault) and also estimated the strike-normal thickness of both the Chugach and Prince William terranes (Figure 1b). These values were compared with subducting Yakutat crustal thickness beneath the margin (from Mann et al., 2022; Figure 3). A sharp change in topography along the major faults at ~149°W corresponds with the point between Yakutat subduction to the east and Pacific plate subduction

382 to the west (Kim et al., 2014; Mann et al., 2022). Additionally, the width of both the Chugach
383 and Prince William terranes decrease to the east, with the Prince William terrane eventually
384 pinching off around the collisional zone at ~141°W (e.g., Chapman et al., 2012) where the
385 subducting Yakutat crustal thickness exceeds 25-30 km (Figure 3). The elevation and terrane
386 width trends indicate significant shortening and deformation across the eastern half of the region,
387 probably related to buoyant Yakutat crust subduction (e.g., Abers, 2008). The west to east
388 transition from low to high deformation at ~149°W is well correlated with the rotation of the
389 BRF to a steeper dip inferred from Sp CCP stacking and previous studies (Enkelmann et al.,
390 2010; Arkle et al., 2013; Mankemthong et al., 2013). As previously described, the similar
391 rotation toward vertical inferred for the Contact Fault (e.g., Fuis et al., 1991) occurs farther east,
392 perhaps indicating that the western limit of the most intense deformation in the more seaward
393 terranes is also offset to the east. This latter conclusion is broadly consistent with the along-strike
394 topographic gradients for the Contact and Chugach-St. Elias Faults (Figure 3).

395 Where the Pacific plate is subducting to the west of the imaged Yakutat plateau
396 (Rondenay et al., 2008; Worthington et al., 2012; Kim et al., 2014; Mann et al., 2022) (i.e., west
397 of ~149°W), the long-term exhumation rate is ~0.1 mm/yr (Valentino et al., 2016), and there has
398 been a minimum of exhumation (< 2-3 km) and inferred shortening since ca. 30 Ma. Arkle et al.
399 (2013) demonstrated, with applied thermochronology, that the Contact Fault is a structural
400 barrier along the central segment (Figure 1), with >11 km of Oligocene-to-Present exhumation
401 north of the fault (exhumation rate of ~0.7 mm/yr) and just a few kilometers of exhumation
402 (exhumation rate of ~0.2 mm/yr) to the south during the same time frame. Hence, the Contact
403 Fault paleo-subduction interface may have played a role in focusing Oligocene-to-Present

404 deformation to the north in this region. Furthermore, in the central segment the BRF paleo-
405 subduction interface was rotated to a subvertical position and also facilitated vertical tectonics
406 (Figure 4). In this scenario the Maastrichtian(?) to Paleogene Contact Fault paleo-subduction
407 interface (Bol and Roeske, 1993; Brocher et al., 1994; Fuis & Plafker, 1991; Davidson & Garver,
408 2017) would be reactivated during the Oligocene-Neogene Yakutat shallow subduction event
409 (e.g., Arkle et al., 2013).

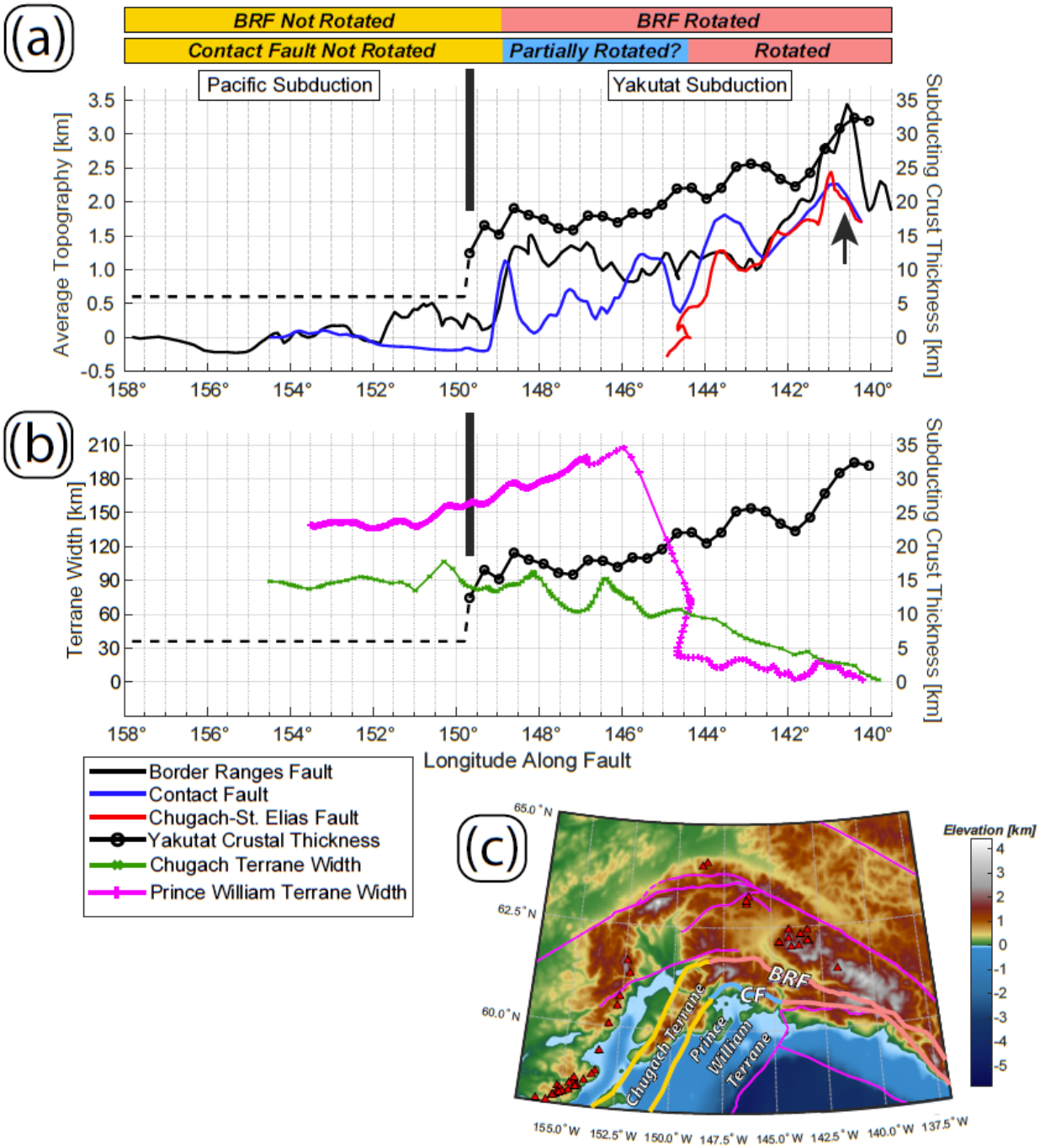

Figure 3: Analysis of topography along the BRF and Contact Fault, and the intervening terranes' approximate thicknesses. It is inferred that the BRF is rotated to subvertical to the east of ~149°W, whereas the Contact Fault is rotated to subvertical to the east of ~145°W. (a) Comparison of subducting Yakutat thickness from Mann et al. (2022) with average topography within 5 km of each fault trace, plotted at the longitude of the fault. Arrow highlights the location of St. Elias syntaxis and collision (Enkelmann et al., 2010, 2015a, 2015b; Chapman et al., 2012) of thickest Yakutat terrane (Worthington et al., 2012; Mann et al., 2022; Brueseke et al., 2023). (b) Comparison of subducting Yakutat thickness with approximate widths of the Prince William and Chugach Terranes. (c) Peach color indicates portions of the Border Ranges and Contact faults that have been rotated to

subvertical. Unrotated sections are denoted by yellow lines. Potentially partially rotated section of Contact Fault is denoted by blue line. These are also shown at top of figure plotted vs longitude. Shades of magenta colouring show offshore Yakutat crustal thickness variations (Worthington et al., 2012).

There is no seismic imaging of the geometry of the Contact Fault east of 145.2°W, but it has been inferred that the fault was rotated towards vertical after ca. 5 Ma (Enkelmann et al., 2008; Chapman et al., 2012). In this region, where both the BRF and Contact Faults have inferred sub-vertical dips, exhumation rates in places are >5 mm/yr (Enkelmann et al., 2015b). The west to east variability in BRF and Contact Faults structural geometry align with known exhumation patterns (Arkle et al., 2013; Valentino et al., 2016; Enkleman et al., 2015b). Low-angle structures are inefficient at exhumation and accommodate contraction more through horizontal than vertical motion (e.g., Reiners and Brandon, 2006), whereas vertical structures facilitate vertical extrusion of crustal blocks (e.g., Benowitz et al., 2022). Overall, the dramatic along-strike variability in structural dip of the BRF and Contact faults implies three different structural configurations operating along the same Oligocene-to-Present trench, aligning with previous work that has highlighted margin-parallel variations in deformation history (Figure 4) (Buscher et al., 2008; Enkelmann et al., 2010; Arkle et al., 2013; Valentino et al., 2016).

5.2.2 Denali and Hines Creek Faults

The upper-plate Moho typically shallows by 5-10 km northward across the Denali Fault system in the profiles analyzed in this study (Figure 2a,b,c,f). The one exception is line D-D', where a shallowing of the Moho across the Denali Fault is more gradual. Crustal thickness of the Yukon-Tanana terrane, which is north of the Denali Fault, is only analyzed along lines of dense station spacing to avoid artifacts due to sparse sampling of the CCP volume. The Moho offset across the Denali Fault system has been imaged by fault-zone head-wave analysis (Allam et al., 2017), RF migration (Allam et al., 2017; Miller et al., 2018; Mann et al., 2022), inversions of

surface-wave data (Haney et al., 2020), joint inversion of RFs and surface-wave data (e.g., Martin-Short et al., 2018; Gama et al., 2022b), and other imaging techniques (for a review, see Yang et al., *this volume*). In the Hines Creek Fault region (Figure 1b), prior studies have found that the crustal thickness step is larger across the Hines Creek Fault than the Denali Fault (e.g., Veenstra et al., 2006; Rossi et al., 2006; Allam et al., 2017; Miller et al., 2018). On the comparable profile from the Sp CCP stack in the study (line C-C'; Figure 2c) the apparent Moho offset actually lies somewhat closer to the Denali Fault than to the Hines Creek Fault, which at this longitude lies ~20 km to the north. However, this difference may reflect the lower horizontal resolution provided by Sp phases, relative to Ps data at a comparable period (e.g., Hansen & Schmandt, 2017; Mancinelli & Fischer, 2017; Hua et al., 2020a; Hua et al., 2020b).

5.2.3 Eureka Creek Fault

The most prominent Moho depth offset imaged across the region in the Sp CCP volume is a ~15-km eastward increase in crustal thickness on line D-D' (Figure 2d) where it crosses the mapped surface trace of the Eureka Creek Fault (Nokleberg et al., 1985). There is also a ~10-km northward increase in crustal thickness across the Eureka Creek Fault along line D-D'. These crustal thickness offsets are very close to the location of newly discovered volcanoes and fissures which lie above the western limb of the tear in the subducting Yakutat slab (Figure 1a) (Brueseke et al., 2023).

The Eureka Creek Fault juxtaposes two significantly different subterranes of the WCT: the Tangle subterrane to the south and the Slana River subterrane to the north (Nokleberg et al., 1985). Not much had been known about the orientation of the Eureka Creek Fault at depth nor its slip-history (e.g., Nokleberg et al., 1985; Nokleberg et al., 1989), but the apparent vertical offset

464 in Moho thickness across the fault is likely an inherited feature from when these two subterranes
465 were juxtaposed across an active strike-slip fault. Overall, the Eureka Creek Fault represents a
466 good example of an ancient subterrane-bounding fault maintaining crustal thickness offsets
467 through time.

468 ***5.2.4 Crustal Structure Beneath Copper River Basin Region***

469 The PVG imaged at ~25-km depth beneath the Copper River Basin extends
470 approximately from 147°W to 145°W, and 62°N to 62.5°N (Figure 2f,g). The maximum
471 thickness of the basin reaches ~2 km (Fuis et al., 1991; Powell et al., 2019), which would result
472 in PVGs at depths <10-km, so this feature is not related to conversions at the base of the basin.
473 However, the PVG does extend throughout the basin and may indicate a link between these
474 features.

475 The mid-crustal PVG is directly above the ca. 1 Ma shallow tear in the subducting
476 Yakutat slab (Figure 5; Mann et al., 2022; Brueseke et al., 2023). A dense cluster of earthquake
477 hypocenters falls at the southeastern boundary of the PVG, near the Klawasi group mud
478 volcanoes (Figure 5; Daly et al., 2021). A NVG follows the PVG at 25-km depth in the
479 southeastern corner, which is especially pronounced beneath the cluster of earthquakes (Figure
480 2g), and finally beneath that is a weak PVG at ~50-km depth which matches the depth where
481 there is a velocity increase in both Ps RF imaging (Mann et al., 2022) and along the TACT lines
482 (e.g., Fuis et al., 1991).

483 Other studies have also found anomalous structures beneath the Copper River Basin. The
484 North-South TACT line through the eastern part of the basin reported compressional velocities
485 of ~6.7-6.9 km/s (e.g., Fuis & Plafker, 1991) below ~20-km depth which more closely match that

of basalt and not continental crust (Brocher, 2005). Refracted P-waves from explosions in College Fjord at the northwest corner of Prince William Sound were recorded traveling at ~6.8 km/s at stations along the Richardson Highway (paralleling line F-F', Figure 2f) but arrived ~1-second delayed along paths crossing this region (Hales & Asada, 1966). This delay was interpreted as resulting from anomalous lower crust and uppermost mantle velocities along these paths and is not the result of Moho depth variations. Additionally, the TACT line extending East-West through the Copper River Basin recorded no Pn or PmP throughout this region, further suggesting the lower crust and uppermost mantle beneath this region are anomalous (Goodwin et al., 1989).

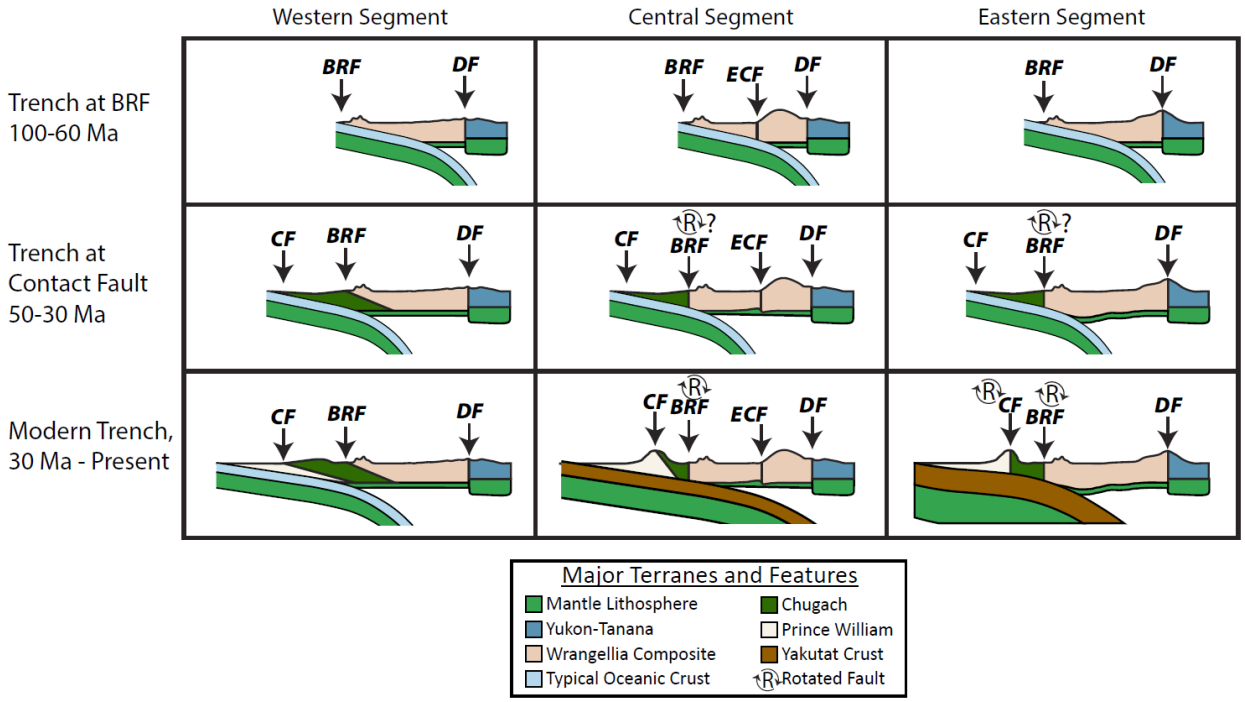

Figure 4: Schematic depicting snapshots through time of each of the three segments (Figure 1c) and whether or not the BRF and/or Contact Fault have been rotated toward subvertical. The central and eastern segments of BRF may have been rotated during ca 60- 50 Ma oblique translation and accretion of the Chugach and Prince William Terrane or this fault rotation from ~15° toward sub-vertical may be related, at least in part, to the Yakutat oceanic plateau subduction. Whereas only the eastern segment of the Contact fault has been rotated from ~15° to ~30° towards subvertical where the Yakutat slab is the thickest (Figure 3). See text for further discussion and references. Note: thicknesses and dip angles in this figure are not drawn to scale.

Based on the TACT active-source experiment results, the region from 20-50 km depth beneath the Copper River Basin was interpreted as having formed from three possible scenarios: (1) North-to-South tectonic underplating of lower North American crust beneath the Wrangellia and Peninsular Terranes, (2) South-to-North tectonic underplating by the Kula plate, or (3) magmatic underplating at some point since the late Cretaceous (Fuis & Plafker, 1991). Tectonic underplating of lower North American crust from the north is not supported by the presence of the sharp offset in crustal thickness across the Eureka Creek faults just to the north of this region (see Section 4.2.3). Such a crustal thickness offset probably would have been obliterated if buoyant lower crust was underthrust southward beneath the region. The subvertical lithospheric-scale nature of the Denali-Hines Creek fault (Gama et al., 2022b; Newell et al., 2023) further discounts scenario (1). Furthermore, the imaged inboard-dipping BRF Mesozoic paleo-subduction interface supports a model of inboard-dipping (east and northward) subduction polarity from the Mesozoic to the Present (Pavlis et al., 2019).

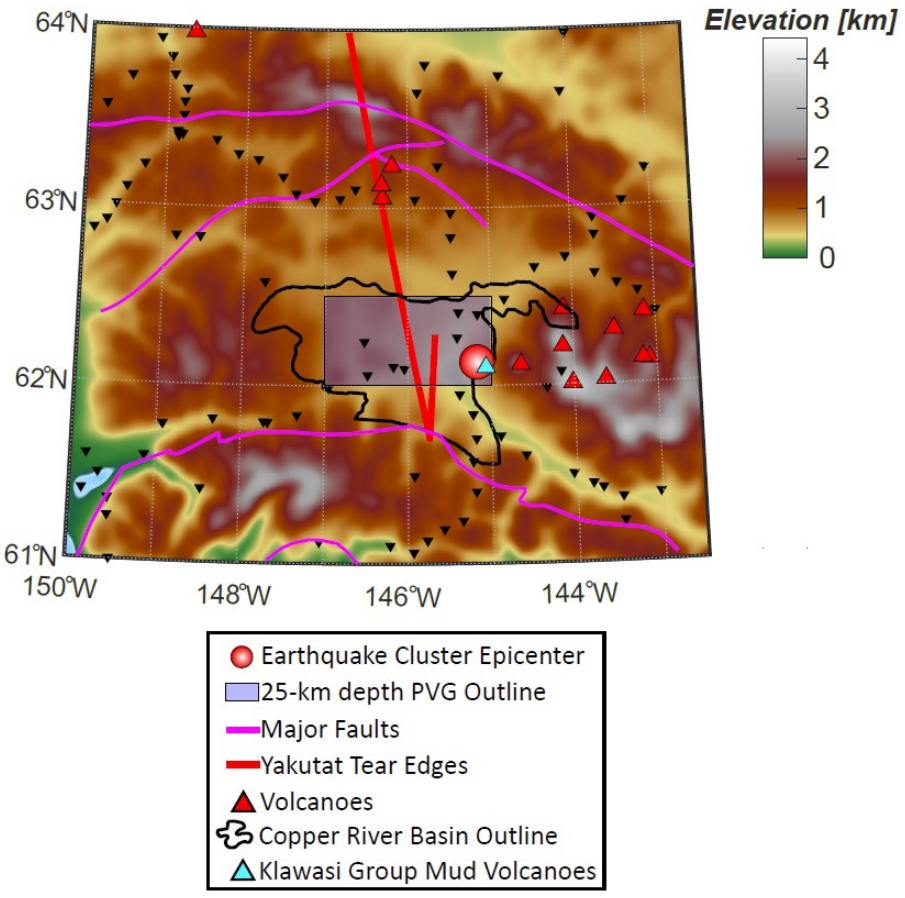

Figure 5: Zoom in of the Copper River Basin and subducting Yakutat slab tear region (outline shown in Figure 1a), highlighting the coincidence of (1) the earthquake cluster at ~25-km depth immediately to the west of the Wrangell Arc (Daly et al., 2021), (2) the PVG seen at ~25-km depth beneath the Copper River Basin, and (3) underlying subducting slab tear location (Mann et al., 2022).

Between the two remaining possible scenarios, (2) and (3), we prefer the interpretation that the source of the subhorizontal mid-crustal PVG is due to magmatic underplating and/or intrusion. The location of this feature abutting against the western limb of the torn Yakutat slab and directly above a nascent slab window (Figure 5; Mann et al., 2022; Brueseke et al., 2023), next to the WVF and below Holocene mud volcanoes, and overlapping with a dense cluster of earthquakes (Daly et al., 2021) suggests a connection between subducting slab tearing, crustal structure, and volcano formation.

This scenario raises interesting questions about crustal thickness across the region. If the sharp PVG at ~25-km depth beneath the Copper River Basin is the base of the Moho, then ponding of basaltic melt into the thin (Gama et al., 2022a) mantle lithosphere of the upper plate may explain the weak underlying PVG at ~50-km depth and the velocities seen in the TACT experiment (Fuis et al., 1991). This scenario would imply that there is a ~20-25-km thick layer of mantle containing ponded melt beneath the upper plate, directly above the tear in the subducting slab. However, if the PVG at ~50-km depth (Figure 2g; Fuis et al., 1991; Ward & Lin, 2018) is the upper plate Moho, then this would require a very large 20-25 km eastward increase in Moho depth within the Copper River Basin to accommodate the shallow Yakutat slab imaged at ~30-km depth on its western end (Figure 2). Maintaining such an abrupt crustal thickness offset over a geologically significant amount of time would be especially challenging in the dynamically active environment created by the subduction of Yakutat crust. Therefore, we prefer the interpretation that the PVG at ~25-km depth is the upper-plate Moho beneath the Tangle subterrane of the WCT (e.g., Nokleberg et al., 1985). This scenario would mean that the reduced velocities in the mantle lithosphere and underlying mantle (i.e., between ~20-50 km depth) seen in active-source results (Fuis et al., 1991), local explosion travel-time analysis (e.g., Hales & Asada, 1966; Goodwin et al., 1989), and recent tomographic results from a joint inversion of RFs and surface wave data (e.g., Ward & Lin, 2018) suggest significant underplating and intrusion of basaltic magmatism into the upper plate, rising from the shallow tear in the subducting Yakutat slab.

All of these features point toward significant alteration of the crust immediately to the west of the Wrangell Volcanic Field and east of the shallow-dipping subducting Yakutat slab

(Figure 5), directly above the tear in the subducting Yakutat slab. A tear or window in a subducting slab would allow for influx of hot asthenospheric mantle into the mantle wedge (e.g., Jadamec & Billen, 2012; Jadamec, 2016; Király et al., 2020) and may rapidly dehydrate and eclogitize subducting crust, leading to significant alterations in the tectonics of the subducting Yakutat slab (e.g., Brueseke et al., 2023), increase in mantle flow (e.g., Jadamec & Billen, 2010), and partial melting rising to the surface which may pond beneath and/or intrude the upper-plate crust. Given the cessation of the westward/northwestward younging age trend and magmatism of the Wrangell Arc at ca. 1 Ma (Richter et al., 1990; Trop et al., 2022), we speculate that the coincidence of the various geophysical observations directly beneath the Klawasi group mud volcanoes just to the west of the youngest Wrangell Arc volcanos (e.g., Sanford, Drum, Wrangell) (Figure 5; Trop et al., 2022) is evidence that these mud volcanos may be signs of growth of the next generation Wrangell Volcanic Field tear volcano.

6. Conclusions

The relatively high-resolution Sp CCP imaging presented here provides one of the best images of crustal architecture across the active Alaskan convergent margin that are free from the effects of reverberations found in Ps RF studies and that sample more widely than active-source studies. This kind of imaging is only possible due to decades of work deploying dense seismometer arrays across the region, which allow for imaging and tracing of upper-plate crustal architecture across the region.

Major findings include:

1) The plate interface is imaged as a NVG above the parallel subducting slab Moho across the Yakutat slab shallow subduction region and agrees well with previous Ps RF imaging.

572 2) This southern Alaska Sp CCP imaging, combined with previous seismic imaging (e.g.,
573 Stephens et al., 1990; Fuis et al., 1991; Ye et al., 1997) and tectonic reconstructions (e.g., Trop
574 and Ridgway, 2007) provide insight into why low-angle paleo-subduction interfaces are
575 preserved in some locations, and rotated toward vertical with time in other places along the
576 margin. The western segment of the BRF preserves the inboard (paleo-east) dipping (~15°)
577 Mesozoic paleo-subduction interface to at least ~25-km depth, but there the BRF may extend
578 further to the upper-plate Moho at ~35-km depth. The next seaward terrane boundary, the
579 Contact Fault between the Chugach Terrane and the Prince William Sound Terrane, is also
580 imaged along the western segment as a shallow dipping (~15°) detachment (e.g., Stephens et al.,
581 1990; Ye et al., 1997). In the central transitional segment, the BRF subduction interface is
582 rotated toward vertical (Figure 2; e.g., Fuis et al., 1991) but the Contact Fault is not (dips ~30°;
583 Fuis et al., 1991), whereas both the BRF and Contact Faults are rotated towards vertical along
584 the eastern segment (Figure 3; Enkelmann et al., 2008; Chapman et al., 2012). These seismic
585 observations in part reflect the differences in Oligocene-to-Present slab thickness between the
586 Pacific and Yakutat segments of the BRF and across-fault lithologic variations. To the east, both
587 the BRF and Contact Fault have been rotated towards vertical where the Yakutat plateau crust is
588 thickest (~25 to 30 km), and this contraction is evidenced by significant shorting across the
589 Prince William Terrane (Figure 3). In summary, Eocene soft-docking of the Chugach and Prince
590 William Terranes via strike-slip faulting (Garver and Davidson, 2015) limited Oligocene-to-
591 Present contraction, and ongoing Pacific slab subduction along the western segment (Buscher et
592 al., 2008; Valentino et al., 2016) has preserved the Mesozoic BRF and the Eocene-Oligocene
593 Contact Fault subduction interface.

3) Discrete upper-plate Moho offsets across terrane (Denali-Hines Creek faults) and sub-terrane (Eureka Creek Fault) boundaries on the order of 10-km highlight significant Mesozoic crustal-scale terrane tectonics. The imaged inboard-dipping BRF Mesozoic paleo-subduction interface supports a model of inboard-dipping (east and northward) subduction polarity from the Mesozoic to the Present (Pavlis et al., 2019), which is also consistent with the upper-plate Moho offsets. 4) We conclude that the newly imaged crust beneath the Copper River Basin, which likely has a thickness of ~25 km, is underplated and significantly magmatically intruded and altered, potentially due to excessive melt rising from the underlying slab tear and ponding beneath the upper plate crust (Daly et al., 2021; Mann et al., 2022). These features and the overlying mud volcanos with mantle fluid isotopic signatures (Motyka et al., 1989) indicate potential for the creation of a new Yakutat slab tear volcano in the Wrangell Volcanic field.

In summary, by applying Sp RF imaging along dense lines of seismometers, we document the preservation of Jura-Cretaceous terrane boundaries and a Mesozoic paleo-subduction interface and the along-strike rotation toward vertical of the same paleo-subduction interface due at least in part to Oligocene-to-Present buoyant Yakutat oceanic plateau subduction. Along-strike variations in subduction zone indenter history and across-strike lithological contrasts are common features of many long-lived convergent margins and the results of this study may have bearing on how inherited crustal features affect later deformation patterns globally.

Acknowledgements

We thank J. Hua for help in implementing the CCP stacking codes. The manuscript was improved through the comments and suggestions of S. Gulick, G. Fuis, and two anonymous

reviewers and benefitted from the foundational work of the USGS Trans-Alaska Crustal Transect (TACT) project. This work was supported by NSF EAR-2053042 and Woods Hole Oceanographic Institution OBS Instrument Center Postdoctoral Scholarship (M. E. M.) and NSF EAR-1829401(K. M. F.).

Data Availability Statement

All data used in this study were obtained from the IRIS Data Management Center (https://ds.iris.edu/ds/nodes/dmc/). IRIS Data Services are funded through the Seismological Facilities for the Advancement of Geoscience and EarthScope (SAGE) Proposal of the National Science Foundation (NSF) under Cooperative Agreement EAR-1261681.

Figure Captions

Figure 6: Overview of study area. (a) Topographic map of study region showing volcanoes and two major sedimentary basins discussed in the text. CIB–Cook Inlet Basin. CRB–Copper River Basin. Outline of Figure 5 is depicted with dashed black lines. (b) Terrane map of study region showing major faults. TiF–Tintina Fault, DF–Denali Fault, HCF–Hines Creek Fault, TaF–Talkeetna Fault, CMF–Castle Mountain Fault, BRF–Border Ranges Fault, CF–Contact Fault, CSEF–Chugach-St. Elias Fault, TrF–Transition Fault, ECF–Eureka Creek Fault. (c) Location of seismic stations used in this study. Outline of Yakutat oceanic plateau shown in shaded gray, with tear highlighted in dark red. Approximate delineation of three segments (i.e., western, central, and eastern) is shown. (d) Weighted ray coverage at 50-km depth in the Sp CCP volume. We only interpret along cross sections where this is greater than 0.4.

Figure 7: Cross sections through the Sp CCP volume analyzed in this study. Negative CCP stack amplitudes correspond to positive velocity gradients (PVG) and positive stack amplitudes correspond to negative velocity gradients (NVG). Each cross section is referenced as its own figure part, corresponding to the first letter each line. For example, line A-A' is "Figure 2a". Small red, blue, and yellow squares plotted on each cross section are from Mann et al. (2022) Ps RF CCP imaging of the subducting Yakutat crust across the same region, using mostly the same seismometers. Small x's are earthquake hypocenters within 5 km of the cross section. Hypocenter locations are from Daly et al. (2021) to the east of 149°W (where they reported high-quality hypocenters), and from the Alaska Earthquake Center catalog to the west of 149°W. The locations where major faults (Figure 1b) cross each cross section are marked with an inverted magenta triangle and label. The locations where the lines cross the Copper River and Cook Inlet basins (Figure 1a) are in tan pentagons, plotted at z = 0 km. All fault labels (black and white lettering) are from Figure 1b. Blue ovals highlight the PVG discussed in Section 5.2.4. Black dashed ovals highlight PVG signal seen dipping inboard from the BRF. Green circles along cross sections denote locations along lines on map in part (i).

Figure 3: Analysis of topography along the BRF and Contact Fault, and the intervening terranes' approximate thicknesses. It is inferred that the BRF is rotated to subvertical to the east of ~149°W, whereas the Contact Fault is rotated to subvertical to the east of ~145°W. (a) Comparison of subducting Yakutat thickness from Mann et al. (2022) with average topography within 5 km of each fault trace, plotted at the longitude of the fault. Arrow highlights the location of St. Elias syntaxis and collision (Enkelmann et al., 2010, 2015a, 2015b; Chapman et al., 2012) of thickest Yakutat terrane (Worthington et al., 2012; Mann et al., 2022; Brueseke et al., 2023). (b) Comparison of subducting Yakutat thickness with approximate widths of the Prince William and Chugach Terranes. (c) Peach color indicates portions of the Border Ranges and Contact faults that have been rotated to subvertical. Unrotated sections are denoted by yellow lines. Potentially partially rotated section of Contact Fault is denoted by blue line. These are also shown at top of figure plotted vs longitude.

Figure 8: Schematic depicting snapshots through time of each of the three segments (Figure 1c) and whether or not the BRF and/or Contact Fault have been rotated toward subvertical. The central and eastern segments of BRF may have been rotated during ca 60- 50 Ma oblique translation and accretion of the Chugach and Prince William Terrane or this fault rotation from

~15° toward sub-vertical may be related, at least in part, to the Yakutat oceanic plateau subduction. Whereas only the eastern segment of the Contact fault has been rotated from ~15° to ~30° towards subvertical where the Yakutat slab is the thickest (Figure 3). See text for further discussion and references. Note: thicknesses and dip angles in this figure are not drawn to scale.

Figure 5: Zoom in of the Copper River Basin and subducting Yakutat slab tear region (outline shown in Figure 1a), highlighting the coincidence of (1) the earthquake cluster at ~25-km depth immediately to the west of the Wrangell Arc (Daly et al., 2021), (2) the PVG seen at ~25-km depth beneath the Copper River Basin, and (3) underlying subducting slab tear location (Mann et al., 2022).

References:

Abers, G. A. (2008). Orogenesis from subducting thick crust and evidence from Alaska, in *Active tectonics and seismic potential of Alaska, geophysical monograph series*. In J. T. Freymueller, et al. (Eds.), (Vol. 179, pp. 337–349). AGU. https://doi.org/10.1029/179GM19

Abers, G. A., MacKenzie, L. S., Rondenay, S., Zhang, Z., Wech, A. G., & Creager, K. C. (2009). Imaging the source region of Cascadia tremor and intermediate-depth earthquakes. *Geology*, *37*(12), 1119–1122. https://doi.org/10.1130/G30143A.1

Allam, A. A., Schulte-Pelkum, V., Ben-Zion, Y., Tape, C., Ruppert, N., & Ross, Z. E. (2017). Ten kilometer vertical Moho offset and shallow velocity contrast along the Denali fault zone from double-difference tomography, receiver functions, and fault zone head waves. *Tectonophysics*, *721*, 56–69. https://doi.org/10.1016/j.tecto.2017.09.003

Alvarado, A., Audin, L., Nocquet, J. M., Jaillard, E., Mothes, P., Jarrín, P., et al. (2016). Partitioning of oblique convergence in the Northern Andes subduction zone: Migration history and the present-day boundary of the North Andean Sliver in Ecuador. *Tectonics*, *35*(5), 1048–1065. https://doi.org/10.1002/2016TC004117

Amand, P.S. (1957). Geological and geophysical synthesis of the tectonics of portions of British Columbia, the Yukon Territory, and Alaska. Geological Society of America Bulletin, 68(10), pp.1343-1370.

Amato, J.M., Pavlis, T.L., Clift, P.D., Kochelek, E.J., Hecker, J.P., Worthman, C.M., & Day, E.M. (2013). Architecture of the Chugach accretionary complex as revealed by detrital zircon ages and lithologic variations: Evidence for Mesozoic subduction erosion in south-central Alaska. *Bulletin*, *125*(11-12), pp.1891-1911.

Arkle, J.C., Armstrong, P.A., Haeussler, P.J., Prior, M.G., Hartman, S., Sendziak, K.L., & Brush, J.A. (2013). Focused exhumation in the syntaxis of the western Chugach Mountains and Prince William Sound, Alaska. *Bulletin*, *125*(5-6), pp.776-793.

Audet, P., Bostock, M. G., Christensen, N. I., & Peacock, S. M. (2009). Seismic evidence for overpressured subducted oceanic crust and megathrust fault sealing. *Nature*, *457*(7225), 76–78. https://doi.org/10.1038/nature07650

Bauer, M. A., Pavlis, G. L., & Landes, M. (2014). Subduction geometry of the Yakutat terrane, southeastern Alaska. *Geosphere*, *10*(6), 1161–1176. https://doi.org/10.1130/GES00852.1

Benowitz, J.A., Roeske, S.M., Regan, S.P., Waldien, T.S., Elliott, J.L., & O'Sullivan, P.B. (2022). Large-scale, crustal-block vertical extrusion between the Hines Creek and Denali faults coeval with slip localization on the Denali fault since ca. 45 Ma, Hayes Range, Alaska, USA. *Geosphere*, *18*(3), pp.1030-1054.

Benowitz, J.A., Davis, K., & Roeske, S. (2019). A river runs through it both ways across time: $^{40}Ar/^{39}Ar$ detrital and bedrock muscovite geochronology constraints on the Neogene

paleodrainage history of the Nenana River system, Alaska Range. *Geosphere*, *15*(3), pp.682-701.

Berger, A.L., Spotila, J.A., Chapman, J.B., Pavlis, T.L., Enkelmann, E., Ruppert, N.A., & Buscher, J.T. (2008). Architecture, kinematics, and exhumation of a convergent orogenic wedge: A thermochronological investigation of tectonic–climatic interactions within the central St. Elias orogen, Alaska. *Earth and Planetary Science Letters*, *270*(1-2), pp.13-24.

Blakely, R. J., Brocher, T. M., & Wells, R. E. (2005). Subduction-zone magnetic anomalies and implications for hydrated forearc mantle. *Geology*, *33*(6), 445. https://doi.org/10.1130/G21447.1

Bostock, M. G., Hyndman, R. D., Rondenay, S., & Peacock, S. M. (2002). An inverted continental Moho and serpentinization of the forearc mantle. *Nature*, *417*(6888), 536–538. https://doi.org/10.1038/417536a

Bol, A.J., & Roeske, S.M. (1993). Strike-slip faulting and block rotation along the contact fault system, eastern Prince William Sound, Alaska. *Tectonics*, *12*(1), pp.49-62.

Brennan, P., Gilbert, H., Ridgway, K. D. (2011), Crustal structure across the central Alaska Range: Anatomy of a Mesozoic collisional zone, *Geochemistry Geophysics Geosystems*, *12*(4).

Brocher, T.M., Fuis, G.S., Fisher, M.A., Plafker, G., Moses, M.J., Taber, J.J., & Christensen, N.I. (1994). Mapping the megathrust beneath the northern Gulf of Alaska using wide-angle seismic data. *Journal of Geophysical Research: Solid Earth*, *99*(B6), pp.11663-11685.

Brocher, T. M. (2005). Empirical Relations between Elastic Wavespeeds, & Density in the Earth's Crust. *Bulletin of the Seismological Society of America*, *95*(6), 2081–2092. https://doi.org/10.1785/0120050077

Brueseke, M. E., Benowitz, J. A., Bearden, A. T., Mann, M. E., & Miggins, D. P. (2023). Subduction disruption, slab tears: ca. 1 Ma true collision of an ~30-km-thick oceanic plateau segment recorded by Yakutat slab nascent tear magmatism. *Terra Nova*, *35*, 49–57. https://doi.org/10.1111/ter.12628

Brueseke, M.E., Benowitz, J.A., Trop, J.M., Davis, K.N., Berkelhammer, S.E., Layer, P.W., & Morter, B.K. (2019). The Alaska Wrangell Arc: ~30 Ma of subduction-related magmatism along a still active arc-transform junction. *Terra Nova*, *31*(1), pp.59-66.

Bruhn, R.L., Pavlis, T.L., Plafker, G., & Serpa, L. (2004). Deformation during terrane accretion in the Saint Elias orogen, Alaska. *Geological Society of America Bulletin*, *116*(7-8), pp.771-787.

Bruhn, R.L., Sauber, J., Cotton, M.M., Pavlis, T.L., Burgess, E., Ruppert, N., & Forster, R.R. (2012). Plate margin deformation and active tectonics along the northern edge of the Yakutat Terrane in the Saint Elias Orogen, Alaska, and Yukon, Canada. *Geosphere*, *8*(6), pp.1384-1407.

Bruns, T. R. (1983). Model for the origin of the Yakutat block, an accreting terrane in the northern Gulf of Alaska. *Geology*, *11*(12), 718. https://doi.org/10.1130/0091-7613(1983)11<718:MFTOOT>2.0.CO;2

Buscher, J.T., Berger, A.L., & Spotila, J.A. (2008). Exhumation in the Chugach-Kenai Mountain belt above the Aleutian subduction zone, southern Alaska. *Washington DC American Geophysical Union Geophysical Monograph Series*, *179*, pp.151-166.

Calvert, A. J., Bostock, M. G., Savard, G., & Unsworth, M. J. (2020). Cascadia low frequency earthquakes at the base of an overpressured subduction shear zone. *Nature Communications*, *11*(1), 3874. https://doi.org/10.1038/s41467-020-17609-3

Chapman, J.B., Pavlis, T.L., Bruhn, R.L., Worthington, L.L., Gulick, S.P., & Berger, A.L. (2012). Structural relationships in the eastern syntaxis of the St. Elias orogen, Alaska. *Geosphere*, *8*(1), pp.105-126.

Christeson, G.L., Gulick, S.P., van Avendonk, H.J., Worthington, L.L., Reece, R.S., & Pavlis, T.L. (2010). The Yakutat terrane: Dramatic change in crustal thickness across the Transition fault, Alaska. *Geology*, *38*(10), pp.895-898..

Christeson, G.L., Van Avendonk, H.J.A., Gulick, S.P.S., Reece, R.S., Pavlis, G.L., & Pavlis, T.L. (2013). Moho interface beneath Yakutat terrane, southern Alaska. *Journal of Geophysical Research: Solid Earth*, *118*(9), pp.5084-5097.

Clark, S.H.B. (1973). The McHugh Complex of south-central Alaska. U.S. Geological Survey Bulletin 1372-D, D1–D11.

Cowan, D.S. (2003). Revisiting the Baranof–Leech River hypothesis for early Tertiary coastwise transport of the Chugach–Prince William terrane. *Earth and Planetary Science Letters*, *213*(3-4), pp.463-475.

Cunningham, E., & Lekić, V. (2019). Constraining crustal structure in the presence of sediment: a multiple converted wave approach. *Geophysical Journal International*, *219*(1), 313–327. https://doi.org/10.1093/gji/ggz298

Daly, K. A., Abers, G. A., Mann, M. E., Roecker, S., & Christensen, D. H. (2021). Subduction of an Oceanic Plateau Across Southcentral Alaska: High-Resolution Seismicity. *Journal of Geophysical Research: Solid Earth*, *126*(11). https://doi.org/10.1029/2021JB022809Davidson, C., & Garver, J.I., 2017. Age and origin of the resurrection ophiolite and associated turbidites of the Chugach–Prince William Terrane, Kenai Peninsula, Alaska. The Journal of Geology, 125(6), pp.681-700.

Eberhart-Phillips, D., Christensen, D.J., Brocher, T.M., Hansen, R., Ruppert, N.A., Haeussler, P.J., & Abers, G.A. (2006). Imaging the transition from Aleutian subduction to Yakutat collision in central Alaska, with local earthquakes and active source data: Journal of Geophysical Research, v. 111, B11303, doi: 10.1029/2005JB004240.

Enkelmann, E., Garver, J.I., & Pavlis, T.L. (2008). Rapid exhumation of ice-covered rocks of the Chugach–St. Elias orogen, Southeast Alaska. *Geology*, *36*(12), pp.915-918.

Enkelmann, E., Zeitler, P.K., Garver, J.I., Pavlis, T.L., & Hooks, B.P. (2010). The thermochronological record of tectonic and surface process interaction at the Yakutat–North American collision zone in southeast Alaska. *American Journal of Science*, *310*(4), pp.231-260.

Enkelmann, E., Koons, P.O., Pavlis, T.L., Hallet, B., Barker, A., Elliott, J., Garver, J.I., Gulick, S.P., Headley, R.M., Pavlis, G.L., & Ridgway, K.D. (2015a). Cooperation among tectonic and surface processes in the St. Elias Range, Earth's highest coastal mountains. *Geophysical Research Letters*, *42*(14), pp.5838-5846.

Enkelmann, E., Valla, P.G., & Champagnac, J.D. (2015b). Low-temperature thermochronology of the Yakutat plate corner, St. Elias Range (Alaska): Bridging short-term and long-term deformation. *Quaternary Science Reviews*, *113*, pp.23-38.

Feng, L., & Ritzwoller, M. H. (2019). A 3-D Shear Velocity Model of the Crust and Uppermost Mantle Beneath Alaska Including Apparent Radial Anisotropy. *Journal of Geophysical Research: Solid Earth*, *124*(10), 10468–10497. https://doi.org/10.1029/2019JB018122

Ferris, A., Abers, G. A., Christensen, D. H., & Veenstra, E. (2003). High resolution image of the subducted Pacific (?) plate beneath central Alaska, 50–150 km depth. *Earth and Planetary Science Letters*, *214*(3–4), 575–588. https://doi.org/10.1016/S0012-821X(03)00403-5

Fisher, M.A. & Magoon, L.B. (1978). Geologic framework of lower Cook inlet, Alaska. *AAPG Bulletin*, *62*(3), pp.373-402.

Fisher, M. A., von Huene, R., Smith, G. L., & Bruns, T. R. (1983). Possible seismic reflections from the downgoing Pacific Plate, 275 kilometers arcward from the Eastern Aleutian Trench. *Journal of Geophysical Research: Solid Earth*, *88*(B7), 5835–5849. https://doi.org/10.1029/JB088iB07p05835

Freeland, G.L. & Dietz, R.S. (1973). Rotation history of Alaskan tectonic blocks. *Tectonophysics*, *18*(3-4), pp.379-389.

Fuis, G. S. & Plafker, G. (1991). Evolution of deep structure along the Trans-Alaska Crustal Transect, Chugach Mountains and Copper River Basin, southern Alaska. *Journal of Geophysical Research: Solid Earth*, *96*(B3), 4229–4253. https://doi.org/10.1029/90JB02276

Fuis, G. S., Ambos, E. L., Mooney, W. D., Christensen, N. I., & Geist, E. (1991). Crustal structure of accreted terranes in southern Alaska, Chugach Mountains and Copper River Basin, from seismic refraction results. *Journal of Geophysical Research: Solid Earth*, *96*(B3), 4187–4227. https://doi.org/10.1029/90JB02316

Fuis, G. S., Moore, T. E., Plafker, G., Brocher, T. M., Fisher, M. A., Mooney, W. D., et al. (2008). Trans-Alaska Crustal Transect and continental evolution involving subduction underplating and synchronous foreland thrusting. *Geology*, *36*(3), 267. https://doi.org/10.1130/G24257A.1

Gama, I., Fischer, K. M., & Hua, J. (2022a). Mapping the Lithosphere and Asthenosphere Beneath Alaska With Sp Converted Waves. *Geochemistry, Geophysics, Geosystems*, *23*(10). https://doi.org/10.1029/2022GC010517

Gama, I., Fischer, K. M., Dalton, C. A., & Eilon, Z. (2022b). Variations in Lithospheric Thickness Across the Denali Fault and in Northern Alaska. *Geophysical Research Letters*, *49*(24). https://doi.org/10.1029/2022GL101256

Garver, J.I. & Davidson, C.M. (2015). Southwestern Laurentian zircons in upper Cretaceous flysch of the Chugach-Prince William terrane in Alaska. *American Journal of Science*, *315*(6), pp.537-556.

Goodwin, E. B., Fuis, G. S., Nokleberg, W. J., & Ambos, E. L. (1989). The crustal structure of the Wrangellia Terrane along the East Glenn Highway, eastern-southern Alaska. *Journal of Geophysical Research: Solid Earth*, *94*(B11), 16037–16057. https://doi.org/10.1029/JB094iB11p16037

Greene, A.R., Scoates, J.S., Weis, D., Katvala, E.C., Israel, S., & Nixon, G.T. (2010). The architecture of oceanic plateaus revealed by the volcanic stratigraphy of the accreted Wrangellia oceanic plateau. *Geosphere*, *6*(1), pp.47-73.

Gulick, S.P., Lowe, L.A., Pavlis, T.L., Gardner, J.V., & Mayer, L.A. (2007). Geophysical insights into the Transition fault debate: Propagating strike slip in response to stalling Yakutat block subduction in the Gulf of Alaska. *Geology*, *35*(8), pp.763-766.

Hales, A. L., & Asada, T. (1966). Crustal Structure in Coastal Alaska. In J. S. Steinhart & T. J. Smith (Eds.), *Geophysical Monograph Series* (pp. 420–432). Washington, D. C.: American Geophysical Union. https://doi.org/10.1029/GM010p0420

Haney, M. M., Ward, K. M., Tsai, V. C., & Schmandt, B. (2020). Bulk Structure of the Crust and Upper Mantle beneath Alaska from an Approximate Rayleigh-Wave Dispersion Formula. *Seismological Research Letters*, *91*(6), 3064–3075. https://doi.org/10.1785/0220200162

Hansen, S. M. & Schmandt, B. (2017). P and S wave receiver function imaging of subduction with scattering kernels. *Geochemistry, Geophysics, Geosystems*, *18*(12), 4487-4502.

Hawkesworth, C., Cawood, P. A., & Dhuime, B. (2019). Rates of generation and growth of the continental crust. *Geoscience Frontiers*, *10*(1), 165–173. https://doi.org/10.1016/j.gsf.2018.02.004

Hopper, E., Fischer, K. M., Wagner, L. S., & Hawman, R. B. (2017). Reconstructing the end of the Appalachian orogeny. *Geology*, *45*(1), 15–18. https://doi.org/10.1130/G38453.1

Hua, J., Fischer, K. M., Wu, M., & Blom, N. A. (2020a). New Approaches to Multifrequency *Sp* Stacking Tested in the Anatolian Region. *Journal of Geophysical Research: Solid Earth*, *125*(11). https://doi.org/10.1029/2020JB020313

Hua, J., Fischer, K. M., Mancinelli, N. J., & Bao, T. (2020b). Imaging with pre-stack migration based on Sp scattering kernels, *Geophys. J. Int.*, *220*, 428-449, https://doi.org/10.1093/gji/ggz459

Hyndman, R. D., & Peacock, S. M. (2003). Serpentinization of the forearc mantle. *Earth and Planetary Science Letters*, *212*(3–4), 417–432. https://doi.org/10.1016/S0012-821X(03)00263-2

Jadamec, M. A., & Billen, M. I. (2010). Reconciling surface plate motions with rapid three-dimensional mantle flow around a slab edge. *Nature*, *465*(7296), 338–341. https://doi.org/10.1038/nature09053

Jadamec, M.A. & Billen, M.I., 2012. The role of rheology and slab shape on rapid mantle flow: Three-dimensional numerical models of the Alaska slab edge. *Journal of Geophysical Research: Solid Earth*, *117*(B2).

Jadamec, M.A., Billen, M.I., & Roeske, S.M., 2013. Three-dimensional numerical models of flat slab subduction and the Denali fault driving deformation in south-central Alaska. *Earth and Planetary Science Letters*, *376*, pp.29-42.

Jadamec, M.A., 2016. Insights on slab-driven mantle flow from advances in three-dimensional modelling. *Journal of Geodynamics*, *100*, pp.51-70.

Kawakatsu, H., Kumar, P., Takei, Y., Shinohara, M., Kanazawa, T., Araki, E., & Suyehiro, K. (2009). Seismic evidence for sharp lithosphere-asthenosphere boundaries of oceanic plates. *Science*, *324*(5926), 499-502.

Kennett, B. L. N. (1991). The Removal of Free Surface Interactions From Three-Component Seismograms. *Geophysical Journal International*, *104*(1), 153–154. https://doi.org/10.1111/j.1365-246X.1991.tb02501.x

Kennett, B. L. N., Engdahl, E. R., & Buland, R. (1995). Constraints on seismic velocities in the Earth from traveltimes. *Geophysical Journal International*, *122*(1), 108–124. https://doi.org/10.1111/j.1365-246X.1995.tb03540.x

Kim, D., Keranen, K. M., Abers, G. A., & Brown, L. D. (2019). Enhanced Resolution of the Subducting Plate Interface in Central Alaska From Autocorrelation of Local Earthquake Coda. *Journal of Geophysical Research: Solid Earth*, *124*(2), 1583–1600. https://doi.org/10.1029/2018JB016167

Kim, Y., Abers, G. A., Li, J., Christensen, D., Calkins, J., & Rondenay, S. (2014). Alaska Megathrust 2: Imaging the megathrust zone and Yakutat/Pacific plate interface in the Alaska subduction zone. *Journal of Geophysical Research: Solid Earth*, *119*(3), 1924–1941. https://doi.org/10.1002/2013JB010581

Király, A., Portner, D.E., Haynie, K.L., Chilson-Parks, B.H., Ghosh, T., Jadamec, M., Makushkina, A., Manga, M., Moresi, L., & O'Farrell, K.A., (2020). The effect of slab gaps on subduction dynamics and mantle upwelling. *Tectonophysics*, *785*, p.228458.

Koons, P.O., Hooks, B.P., Pavlis, T., Upton, P., & Barker, A.D., (2010). Three-dimensional mechanics of Yakutat convergence in the southern Alaskan plate corner. *Tectonics*, *29*(4).

Korja, A., & Heikkinen, P. J. (2008). Seismic images of Paleoproterozoic microplate boundaries in the Fennoscandian Shield. In *Special Paper 440: When Did Plate Tectonics Begin on Planet Earth?* (Vol. 440, pp. 229–248). Geological Society of America. https://doi.org/10.1130/2008.2440(11)

Krueger, H. E., Gama, I., & Fischer, K. M. (2021). Global Patterns in Cratonic Mid-Lithospheric Discontinuities From Sp Receiver Functions. *Geochemistry, Geophysics, Geosystems, 22*(6). https://doi.org/10.1029/2021GC009819

Kumar, P., & Kawakatsu, H. (2011). Imaging the seismic lithosphere-asthenosphere boundary of the oceanic plate: OCEANIC LAB IMAGING. *Geochemistry, Geophysics, Geosystems*, *12*(1), n/a-n/a. https://doi.org/10.1029/2010GC003358

Kusky, T.M., Glass, A.,, & Bradley, D.C. (2007). Structure, Cr-chemistry, and age of the Border Ranges ultramafic/mafic complex: A suprasubductionzone ophiolite complex. In: Ridgway, K.D., Trop, J., Glen, M.,, & O'Neill, J.M. (eds) Tectonic Growth of a Collisional Continental Margin: Crustal Evolution of Southern Alaska. Geological Society of America, Special Papers, 431, 207–225.

Langston, C. A. (1977). Corvallis, Oregon, crustal and upper mantle receiver structure from teleseismic *P* and *S* waves. *Bulletin of the Seismological Society of America*, *67*(3), 713–724. https://doi.org/10.1785/BSSA0670030713

Lekić, V., French, S. W., & Fischer, K. M. (2011). Lithospheric Thinning Beneath Rifted Regions of Southern California. *Science*, *334*(6057), 783–787. https://doi.org/10.1126/science.1208898

Lekić, V. & Fischer, K. M. (2017). Interpreting spatially stacked Sp receiver functions. *Geophysical Journal International*, *210*(2), 874-886

Li, J., Abers, G. A., Kim, Y., & Christensen, D. (2013). Alaska megathrust 1: Seismicity 43 years after the great 1964 Alaska megathrust earthquake. *Journal of Geophysical Research: Solid Earth*, *118*(9), 4861–4871. https://doi.org/10.1002/jgrb.50358

Li, C., Gao, H., & Williams, M. L. (2020). Seismic characteristics of the eastern North American crust with Ps converted waves: Terrane accretion and modification of continental crust. *Journal of Geophysical Research: Solid Earth*, *125*, e2019JB018727. https://doi.org/10.1029/2019JB018727

Little, T. A., & Naeser, C. W. (1989). Tertiary tectonics of the Border Ranges Fault System, Chugach Mountains, Alaska: Deformation and uplift in a forearc setting. *Journal of Geophysical Research: Solid Earth*, *94*(B4), 4333–4359. https://doi.org/10.1029/JB094iB04p04333

Long, M. D., Benoit, M. H., Aragon, J. C., & King, S. D. (2019). Seismic imaging of mid-crustal structure beneath central and eastern North America: Possibly the elusive Grenville deformation? *Geology*, *47*(4), 371-374.

MacKevett, E.M. & Plafker, G. (1974). The Border Ranges fault in south-central Alaska. *US Geological Survey Journal of Research*, *2*, pp.323-329.

Mancinelli, N. J. & Fischer, K. M. (2017). The spatial sensitivity of Sp converted waves---Scattered wave kernels and their applications to receiver-function migration and inversion, *Geophys. J. Int.*, *212*, 1722–1735, https://doi.org/10.1093/gji/ggx506

Mankhemthong, N., Doser, D. I., & Pavlis, T. L. (2013). Interpretation of gravity and magnetic data and development of two-dimensional cross-sectional models for the Border Ranges fault system, south-central Alaska. *Geosphere*, *9*(2), 242–259. https://doi.org/10.1130/GES00833.1

Mann, M. E., Abers, G. A., Daly, K. A., & Christensen, D. H. (2022). Subduction of an Oceanic Plateau Across Southcentral Alaska: Scattered-Wave Imaging. *Journal of Geophysical Research: Solid Earth*, *127*(1). https://doi.org/10.1029/2021JB022697

Margirier, A., Strecker, M. R., Reiners, P. W., Thomson, S. N., Casado, I., George, S. W. M., & Alvarado, A. (2023). Late Miocene Exhumation of the Western Cordillera, Ecuador, Driven by Increased Coupling Between the Subducting Carnegie Ridge and the South American Continent. *Tectonics*, *42*(1). https://doi.org/10.1029/2022TC007344

Martin-Short, R., Allen, R., Bastow, I. D., Porritt, R. W., & Miller, M. S. (2018). Seismic Imaging of the Alaska Subduction Zone: Implications for Slab Geometry and Volcanism. *Geochemistry, Geophysics, Geosystems*, *19*(11), 4541–4560. https://doi.org/10.1029/2018GC007962

Miller, M. S., O'Driscoll, L. J., Porritt, R. W., & Roeske, S. M. (2018). Multiscale crustal architecture of Alaska inferred from P receiver functions. *Lithosphere*, *10*, 267-278. 1050 doi: 10.1130/L701.1.

Motyka, R.J., Poreda, R.J., & Jeffrey, A.W. (1989). Geochemistry, isotopic composition, and origin of fluids emanating from mud volcanoes in the Copper River basin, Alaska. *Geochimica et Cosmochimica Acta*, *53*(1), pp.29-41.

Newell, D.L, Benowitz, J.A., Regen, S.P., Hiett, C.D., (2023). Roadblocks and speed limits: Mantle-to-surface volatile flux through the lithospheric-scale Denali fault, Alaska: Geology, v. 51, p. 576–580, https://doi.org/10.1130/G51068.1

Nilsen, T.H. & Zuffa, G.G. (1982). The Chugach terrane, a Cretaceous trench-fill deposit, southern Alaska. *Geological Society, London, Special Publications*, *10*(1), pp.213-227.

Nokleberg, W. J., Jones, D. L., & Silberling, N. J. (1985). Origin and tectonic evolution of the Maclaren and Wrangellia terranes, eastern Alaska Range, Alaska. *Geological Society of America Bulletin*, *96*(10), 1251. https://doi.org/10.1130/0016-7606(1985)96<1251:OATEOT>2.0.CO;2

975 Nokleberg, W. J., Foster, H. L., & Aleinikoff, J. N. (1989). Geology of the northern Copper
976 River basin, eastern Alaska range, and southern Yukon-Tanana Upland. In W. J.
977 Nokleberg & M. A. Fisher (Eds.), *Alaskan Geological and Geophysical Transect* (pp.
978 34–63). Washington, D. C.: American Geophysical Union.
979 https://doi.org/10.1029/FT104p0034

980 Pavlis, T.L. (1982). Origin and age of the Border Ranges fault of southern Alaska and its bearing
981 on the late Mesozoic tectonic evolution of Alaska. *Tectonics*, *1*(4), pp.343-368.

982 Pavlis, T.L., Picornell, C., Serpa, L., Bruhn, R.L., & Plafker, G. (2004). Tectonic processes
983 during oblique collision: Insights from the St. Elias orogen, northern North American
984 Cordillera. *Tectonics*, *23*(3).

985 Pavlis, T. L., & Roeske, S. M. (2007). The Border Ranges fault system, southern Alaska. In
986 *Special Paper 431: Tectonic Growth of a Collisional Continental Margin: Crustal*
987 *Evolution of Southern Alaska* (Vol. 431, pp. 95–127). Geological Society of America.
988 https://doi.org/10.1130/2007.2431(05)

989 Pavlis T.L., Chapman JB, Bruhn R.L., Ridgway K, Worthington LL, Gulick S.P.,, & Spotila J.
990 (2012). Structure of the actively deforming fold-thrust belt of the St. Elias orogen with
991 implications for glacial exhumation and three-dimensional tectonic processes. *Geosphere*.
992 2012 Oct 1;8(5):991-1019.

993 Pavlis, T.L., Amato, J.M., Trop, J.M., Ridgway, K.D., Roeske, S.M., & Gehrels, G.E. (2019).
994 Subduction polarity in ancient arcs: A call to integrate geology and geophysics to
995 decipher the Mesozoic tectonic history of the northern Cordillera of North America: *GSA*
996 *Today*, no. 11, v. 29, https://doi.org/10.1130/GSATG402A.1

997 Peacock, S. M., Christensen, N. I., Bostock, M. G., & Audet, P. (2011). High pore pressures and
998 porosity at 35 km depth in the Cascadia subduction zone. *Geology*, *39*(5), 471–474.
999 https://doi.org/10.1130/G31649.1

1000 Plafker, G., Nokleberg, W. J., Lull, J. S. (1989). Bedrock geology and tectonic evolution of the
1001 Wrangellia, Peninsular, and Chugach Terranes along the Trans-Alaska Crustal Transect
1002 in the Chugach Mountains and Southern Copper River Basin, Alaska. *Journal of*
1003 *Geophysical Research: Solid Earth, 94*(B4), 4255-4295.

1004 Plafker, G. & Berg, H. C. (1994). Overview of the geology and tectonic evolution of Alaska. *The*
1005 *Geology of North America, GSA, Chapter 33,* 989-1021.

1006 Powell, Doug, & Amoco Oil Co. (2019), Geological report to the Ahtna Corporation, Copper
1007 River basin, Alaska, 1975: Alaska Division of Geological & Geophysical Surveys
1008 Geologic Materials Center Data Report 455, 26 p., 9 sheets.
1009 https://doi.org/10.14509/30324

1010 Reiners, P.W. & Brandon, M.T. (2006). Using thermochronology to understand orogenic
1011 erosion. *Annu. Rev. Earth Planet. Sci*., 34, pp.419-466.

Richter, D.H., Smith, J.G., Lanphere, M.A., Dalrymple, G.B., Reed, B.L., & Shew, N. (1990). Age and progression of volcanism, Wrangell volcanic field, Alaska. *Bulletin of Volcanology*, *53*, pp.29-44.

Ridgway, K.D., Trop, J.M., Nokleberg, W.J., Davidson, C.M., & Eastham, K.R. (2002). Mesozoic and Cenozoic tectonics of the eastern and central Alaska Range: Progressive basin development and deformation in a suture zone. *Geological Society of America Bulletin*, *114*(12), pp.1480-1504.

Rondenay, S. (2009). Upper mantle imaging with array recordings of converted and scattered teleseismic waves. Surveys in Geophysics, 30(4–5), 377–405. https://doi.org/10.1007/s10712-009-9071-5

Rondenay, S., Abers, G. A., & van Keken, P. E. (2008). Seismic imaging of subduction zone metamorphism. *Geology*, *36*(4), 275. https://doi.org/10.1130/G24112A.1

Rossi, G., Abers, G. A., Rondenay, S., & Christensen, D. H. (2006). Unusual mantle Poisson's ratio, subduction, and crustal structure in central Alaska. *Journal of Geophysical Research*, *111*(B9), B09311. https://doi.org/10.1029/2005JB003956

Saltus, R. W., & Hudson, T. L. (2022). There is more Wrangellia — magnetic characterization of southern Alaska crust. *Canadian Journal of Earth Sciences*, *59*(4), 243–257. https://doi.org/10.1139/cjes-2020-0209

Sato, H., Kato, N., Abe, S., Van Horne, A., & Takeda, T. (2015). Reactivation of an old plate interface as a strike-slip fault in a slip-partitioned system: Median Tectonic Line, SW Japan. *Tectonophysics*, *644–645*, 58–67. https://doi.org/10.1016/j.tecto.2014.12.020

Schartman, A., Enkelmann, E., Garver, J.I., & Davidson, C.M. (2019). Uplift and exhumation of the Russell Fiord and Boundary blocks along the northern Fairweather transform fault, Alaska. *Lithosphere*, *11*(2), pp.232-251.

Sheehan, A. F., Abers, G. A., Jones, C. H., & Lerner-Lam, A. L. (1995). Crustal thickness variations across the Colorado Rocky Mountains from teleseismic receiver functions. *Journal of Geophysical Research: Solid Earth*, *100*(B10), 20391–20404. https://doi.org/10.1029/95JB01966

Shellenbaum, D. P., L. S. Gregersen,, & P. R. Delaney (2010). Top Mesozoic unconformity depth map of the Cook Inlet basin, Alaska, *Rept. Investig. 2010-2*, Alaska Division of Geological and Geophysical Surveys, Fairbanks, Alaska.

Smart, K.J., Pavlis, T.L., Sisson, V.B., Roeske, S.M., & Snee, L.W., (1996), The Border Ranges fault system in Glacier Bay National Park, Alaska: evidence for major early Cenozoic dextral strike-slip motion, *Canadian Journal of Earth Sciences*, *33*(9), pp.1268-1282.

Smith, K., & Tape, C. (2020). Seismic Response of Cook Inlet Sedimentary Basin, Southern Alaska. *Seismological Research Letters*, *91*(1), 33–55. https://doi.org/10.1785/0220190205

1049 Spotila, J.A. & Berger, A.L. (2010). Exhumation at orogenic indentor corners under long-term
1050 glacial conditions: Example of the St. Elias orogen, Southern Alaska. *Tectonophysics*,
1051 *490*(3-4), pp.241-256.

1052 Stephens, C. D., Page, R. A., & Lahr, J. C. (1990). Reflected and mode-converted seismic waves
1053 within the shallow Aleutian Subduction Zone, Southern Kenai Peninsula, Alaska. *Journal*
1054 *of Geophysical Research*, *95*(B5), 6883. https://doi.org/10.1029/JB095iB05p06883

1055 Tape, C., Christensen, D., Moore-Driskell, M. M., Sweet, J., & Smith, K. (2017). Southern
1056 Alaska Lithosphere and Mantle Observation Network (SALMON): A Seismic
1057 Experiment Covering the Active Arc by Road, Boat, Plane, and Helicopter.
1058 *Seismological Research Letters*, *88*(4), 1185–1202. https://doi.org/10.1785/0220160229

1059 Terhune, P.J., Benowitz, J.A., Trop, J.M., O'Sullivan, P.B., Gillis, R.J., & Freymueller, J.T.,
1060 (2019), Cenozoic tectono-thermal history of the southern Talkeetna Mountains, Alaska:
1061 Insights into a potentially alternating convergent and transform plate margin, *Geosphere*,
1062 *15*(5), pp.1539-1576.
1063 Tikoff, B., Housen, B. A., Maxson, J. A., Nelson, E. M., Trevino, S., & Shipley, T. F. (2023).
1064 Hit-and-run model for Cretaceous–Paleogene tectonism along the western margin of
1065 Laurentia. In S. J. Whitmeyer, M. L. Williams, D. A. Kellett, & B. Tikoff, *Laurentia:*
1066 *Turning Points in the Evolution of a Continent* (pp. 659–705). Geological Society of
1067 America. https://doi.org/10.1130/2022.1220(32)

1068 Trop, J.M., Benowitz, J.A., Kirby, C.S., & Brueseke, M.E. (2022). Geochronology of the
1069 Wrangell Arc: Spatial-temporal evolution of slab-edge magmatism along a flat-slab,
1070 subduction-transform transition, Alaska-Yukon. *Geosphere*, *18*(1), pp.19-48.

1071 Trop, J.M., Benowitz, J.A., Koepp, D.Q., Sunderlin, D., Brueseke, M.E., Layer, P.W., &
1072 Fitzgerald, P.G., (2020). Stitch in the ditch: Nutzotin Mountains (Alaska) fluvial strata
1073 and a dike record ca. 117–114 Ma accretion of Wrangellia with western North America
1074 and initiation of the Totschunda fault. *Geosphere*, *16*(1), pp.82-110.

1075 Trop, J. M., Benowitz, J., Cole, R. B., & O'Sullivan, P. (2019), Cretaceous to Miocene
1076 magmatism, sedimentation, and exhumation within the Alaska Range suture zone: A
1077 polyphase reactivated terrane boundary, *Geosphere*, *15*(4), pp.1066-1101.

1078 Trop, J. M., & Ridgway, K. D. (2007). Mesozoic and Cenozoic tectonic growth of southern
1079 Alaska: A sedimentary basin perspective. In *Special Paper 431: Tectonic Growth of a*
1080 *Collisional Continental Margin: Crustal Evolution of Southern Alaska* (Vol. 431, pp. 55–
1081 94). Geological Society of America. https://doi.org/10.1130/2007.2431(04)

1082 Valentino, J. D., Spotila, J. A., Owen, L. A., & Buscher, J. T. (2016). Rock uplift at the transition
1083 from flat-slab to normal subduction: The Kenai Mountains, Southeast Alaska.
1084 *Tectonophysics*, *671*, 63–75. https://doi.org/10.1016/j.tecto.2016.01.022

1085 Veenstra, E., Christensen, D. H., Abers, G. A., & Ferris, A. (2006). Crustal thickness variation in
1086 south-central Alaska. *Geology*, *34*(9), 781. https://doi.org/10.1130/G22615.1

Ward, K. M., & Lin, F. (2018). Lithospheric Structure Across the Alaskan Cordillera From the Joint Inversion of Surface Waves and Receiver Functions. *Journal of Geophysical Research: Solid Earth*, *123*(10), 8780–8797. https://doi.org/10.1029/2018JB015967

Westerweel, J., Roperch, P., Licht, A., Dupont-Nivet, G., Win, Z., Poblete, F., et al. (2019). Burma Terrane part of the Trans-Tethyan arc during collision with India according to palaeomagnetic data. *Nature Geoscience*, *12*(10), 863–868. https://doi.org/10.1038/s41561-019-0443-2

Worthington, L.L., Van Avendonk, H.J., Gulick, S.P., Christeson, G.L., & Pavlis, T.L., 2012. Crustal structure of the Yakutat terrane and the evolution of subduction and collision in southern Alaska. *Journal of Geophysical Research: Solid Earth*, *117*(B1).

Ye, S., Flueh, E. R., Klaeschen, D., & Huene, R. (1997). Crustal structure along the EDGE transect beneath the Kodiak shelf off Alaska derived from OBH seismic refraction data. *Geophysical Journal International*, *130*(2), 283–302. https://doi.org/10.1111/j.1365-246X.1997.tb05648.x

Zhang, Y., Li, A., & Hu, H. (2019). Crustal structure in Alaska from receiver function analysis. *Geophysical Research Letters*, *46*, 1284-1292. https://doi.org/10.1029/2018GL081011